

---

**Where Has All the Energy Gone?  
Quantifying Advective Energy  
Fluxes with Dense Tower Networks**

---

Emily R. Mather

A Thesis submitted in partial fulfillment of  
the requirements for the degree of

Master of Science

(Atmospheric and Oceanic Sciences)

at the

UNIVERSITY OF WISCONSIN-MADISON

October 2024

# Abstract

## Where Has All the Energy Gone? Quantifying Advective Energy Fluxes

### with Dense Tower Networks

by Emily R. Mather

Accurate and extensive measurements of the exchange of energy between the land surface and atmosphere are needed for building and improving models of the earth's climate system. The eddy covariance (EC) method, used to measure the exchange of energy and gasses between the land surface and atmosphere, consistently measures an imbalance in the surface-atmosphere energy budget with greater incoming energy fluxes than outgoing fluxes. Studies have suggested that large-scale secondary circulations (SCs) may be responsible for some of the energy transport that is not measured by EC systems. This missing portion of the energy budget may be captured by quantifying the advective energy fluxes with dense tower networks. In this study, we investigated whether, and under what conditions, advective fluxes of sensible and latent heat may be estimated from a high-density network of tower measurements such as those taken during the CHEESEHEAD19 experiment. We applied horizontal and vertical interpolation methods to measurements of temperature and humidity in order to calculate x,y, and z gradients across each EC measurement site within the CHEESEHEAD19 domain. These gradients were used, in addition to wind measurements, to quantify horizontal and vertical advective energy fluxes. Inclusion of the advective fluxes did not consistently improve energy budget closure, indicating that our method fails to provide accurate estimates of advective energy

transport. Results suggest that a greater spatial density of measurements and an alternative vertical velocity measurement method may allow for improved advection estimates from a similar tower network. While this work lends insight into the nature of advective energy transport over heterogeneous land surfaces, further investigation is needed to improve our understanding of the contribution of advective fluxes to the surface-atmosphere energy balance.

# Acknowledgements

I would like to express my sincere gratitude to my advisor, Dr. Ankur Desai, for taking me on as a grad student and for the support, mentorship, and guidance over the past two and half years. Thank you for all of the knowledge, wisdom, and science-world insider tips you have shared with me. I would further like to thank my committee members, Tristan L'Ecuyer and Paul Stoy, for their academic advice throughout my time in grad school and for their constructive feedback on my thesis. Thank you to Bethany Blakely for serving as an informal mentor to me and for keeping science fun.

Thank you to my mom, Karla, for encouraging me to dream of big things, to my dad, Randy, for reminding me not to forget the small details, and to both for all of your love and support. To my sisters Anna and Sarah, thank you both for being great listeners and keeping me both grounded and on my toes. To my friends, in Madison and beyond, thank you for reminding me that there is a world outside of grad school and for bringing so much joy to my life. Thank you to my partner Sam for being by my side through the hardest days of writing this thesis, for making sure I had delicious food to look forward to at the end of those days, and for always being willing to listen to me talk about flux towers.

Finally, I wish to acknowledge all of the teachers and professors who have played a part in my academic journey thus far. I have been encouraged and inspired by so many incredible educators over the years and have them to thank for shaping me into the student and scientist I am today.

# Contents

<b>Abstract</b>	<b>i</b>
<b>Acknowledgements</b>	<b>iii</b>
<b>Contents</b>	<b>iv</b>
<b>List of Figures</b>	<b>vi</b>
<b>List of Tables</b>	<b>ix</b>
<b>1 Introduction</b>	<b>1</b>
1.1 Surface-atmosphere energy budget . . . . .	2
1.2 Issues affecting energy balance closure . . . . .	3
1.2.1 Data collection and processing errors . . . . .	4
1.2.2 Additional energy fluxes . . . . .	6
1.2.2.1 Storage . . . . .	10
1.2.2.2 Horizontal Advection . . . . .	11
1.2.2.3 Vertical Advection . . . . .	12
1.2.2.4 Relationship between advective flux components . . . . .	15
1.2.3 Conditions associated with Energy Imbalance . . . . .	16
1.3 Research Objectives . . . . .	17
<b>2 Data and Methods</b>	<b>19</b>
2.1 The CHEESEHEAD19 Experiment . . . . .	19
2.2 Data Used . . . . .	20
2.3 Advection Quantification . . . . .	22
2.3.1 Horizontal Advection . . . . .	22
2.3.2 Vertical Advection . . . . .	26
2.4 Energy Balance Analysis . . . . .	28
2.5 Case Evaluation . . . . .	29
2.6 Sensitivity Analysis . . . . .	30
2.6.1 Wind Profiles . . . . .	31
2.6.2 Horizontal Gradients . . . . .	32

	v
2.6.2.1	Horizontal Interpolation Variations . . . . . 32
2.6.2.2	Gradient Averaging Method . . . . . 33
2.6.3	Vertical Velocity Estimates . . . . . 35
<b>3</b>	<b>Results</b> . . . . . <b>38</b>
3.1	Estimates of Advective Energy Fluxes . . . . . 38
3.2	Relationships between advective flux components . . . . . 40
3.3	Effect of Environmental Conditions on Advective Fluxes . . . . . 43
3.4	Contribution of Advective Fluxes to Energy Budget Closure . . . . . 47
3.5	Case Evaluation . . . . . 48
3.6	Sensitivity to calculation method . . . . . 52
<b>4</b>	<b>Discussion</b> . . . . . <b>57</b>
4.1	Estimates of advective fluxes . . . . . 58
4.2	Relationships between advective flux components . . . . . 60
4.3	Effect of environmental conditions on advective energy fluxes . . . . . 62
4.4	Contribution of advective fluxes to energy budget closure . . . . . 64
4.5	Sensitivity to calculation method . . . . . 65
<b>5</b>	<b>Conclusion</b> . . . . . <b>68</b>
<b>A</b>	<b>Complete List of Cases</b> . . . . . <b>71</b>
	<b>Bibliography</b> . . . . . <b>81</b>

# List of Figures

1.1	Diel cycle of measured energy balance components from the CHEESEHEAD19 dataset. Values are average across all days and measurement sites. . . . .	4
1.2	Time series of vertical wind velocity from 16:00-19:00 local time on August 20, 2019 at NE1 tower. 20 Hz measurements are shown in blue with the 30 minute average in red. . . . .	13
2.1	Map of CHEESEHEAD19 tower locations. Coordinates are given in degrees E and degrees N. . . . .	21
2.2	Map of CHEESEHEAD19 domain showing horizontal interpolation method and wind directions. Black dots mark the flux towers where $T$ and $q$ were directly measured. Arrows show the wind direction measured at each tower. Xs mark the upwind (blue) and downwind (red) points to which $T$ and $q$ were interpolated. . . . .	25
2.3	Left: Example vertical profile of $T$ at the NW1 tower determined by linearly interpolating measurements taken at the point marked by blue dots. Right: Profile from SW2 tower showing that $T$ was linearly extrapolated to 33 m for use in the horizontal interpolation. Both profiles from 18:00 local time on July 20, 2019. . . . .	27
2.4	Time series of total advective energy flux (gray) and energy imbalance (black), showing the two case evaluation periods: P1 in blue and P2 in red. . . . .	30
2.5	Decision tree diagram of calculation variation used in sensitivity analysis. . . . .	31
3.1	Histograms showing distribution of half-hourly flux values for each advective flux component. Components shown are, clockwise from top left, $H_{HA}$ , $\lambda E_{HA}$ , $\lambda E_{VA}$ , and $H_{VA}$ . . . . .	40
3.2	Scatter plots of horizontal versus vertical advective fluxes of sensible (left) and latent (right) heat. Points are semi-transparent so that the darker areas represent a greater density of points. Best-fit lines are shown in red. Plot ranges have been restricted, cutting off some outliers in order to show the center of the plot in more detail. . . . .	41

3.3	Scatter plot of the Bowen ratios of turbulent vs. advective fluxes. The best fit line is shown in red. The black line has a slope of one, indicating the one-to-one relationship between turbulent and advective Bowen ratios which is assumed by the Bowen ratio closure method. . . . .	42
3.4	Average diel cycle of advective fluxes of latent and sensible heat for each tower in gray. Two towers are highlighted in color as examples of the differing sign of the midday peak of $\lambda E_{HA}$ and $\lambda E_{VA}$ . Tower NE1 is shown in blue and SW3 in red. . . . .	44
3.5	7 day averaged total advection and available energy over the course of the CHEESEHEAD19 experiment. Regression lines are shown in red with the equation of the line given in the upper right-hand corner. In the regression equations, x represents the number of days since the start of the experiment, June 20th. . . . .	45
3.6	Top: Box plot showing relationship between stability parameter ( $z/L$ ) and total advective flux. Advective fluxes were grouped by $z/L$ value. $z/L$ bins edges were set according to the percentiles such that 10% of measurements fall into each bin. Bottom: same as top but with friction velocity ( $u_*$ ) in place of $z/L$ . . . . .	46
3.7	Scatter plot of mean $Imb_{NA}$ vs. $Imb_A$ for each tower. Blue region bounded by dashed lines represents an improvement in energy balance closure as defined by the absolute value of $Imb_A$ being lower than $Imb_{NA}$ . . . . .	48
3.8	Percent of site-hours when energy balance was improved (blue), relatively unchanged (gray), or made worse (red) by the inclusion of advective energy fluxes. Unchanged site-hours defined as a change of less than 10% of $Imb_{NA}$ . . . . .	49
3.9	Scatter plot of $Imb$ vs. total advective flux for P1 (blue) and P2 (red). Best fit lines for each period are shown as dashed lines in the same color as the scatter plot points. . . . .	50
3.10	$Imb_{NA}$ and $Imb_A$ for P1 and the entire extent of CHEESEHEAD study. $Imb$ values are shown for 7 towers which had data for at least 75% of timesteps during P1: NE1, NW4, NE2, NE4, SW2, and SW3 . . . . .	51
3.11	Same as Figure 3.2, except only for NE1P1. . . . .	52
3.12	Same as Figure 3.3, except only for NE1P1. . . . .	53
3.13	Scatter plots of horizontal advective fluxes for each half-hour measurement period for case A v. each case variation listed in Table 2.2. Bottom right panel shows vertical advection using sonic anemometer-derived $\bar{w}$ v. vertical advection from continuity. Regression lines are shown in black on all plots. . . . .	55
3.14	Average diel cycle of total advective energy flux for each of the 204 calculation variations (as outlined in Figure 2.5). Advection estimates using sonic-derived $\bar{w}$ are shown in blue while estimates from continuity-derived $\bar{w}$ are shown in red. . . . .	56

4.1	Scatter plot of distance from each tower to the nearest tower vs. total horizontal advective energy flux ( $H_{HA} + \lambda E_{HA}$ ). Regression line shown in red. . . . .	60
-----	---	----

# List of Tables

2.1	AGL Sensor heights for $T$ and $q$ measurements for each tower as well as ASL elevation for the lowest measurement level. All measurements in m. Values with asterisks indicate measurement levels that were too far from others to be treated as if in the same horizontal plane, as described in section 2.3.1 . . . . .	22
2.2	Subset of the horizontal advection calculation variations. Case A is the primary method. Cells with asterisks indicate where each case differs from case A. . . . .	37
3.1	Median values of each component and total advective fluxes for each tower. Values in parentheses are medians of advective fluxes as percentages of available energy. . . . .	39
A.1	List of all advective flux variations tested. . . . .	80

# Chapter 1

## Introduction

Energy exchange between the land surface and atmosphere is an important driver of weather and climate. In particular, characteristics of the land surface influence the partitioning of energy into sensible and latent heat, which in turn, influences the structure and dynamics of the atmospheric boundary layer (Pielke et al., 1998). Accurate and extensive measurements of surface-atmosphere energy fluxes are needed for improving the realism of weather and climate models (Fisher and Koven, 2020). However, measuring all the components of the surface energy budget remains a scientific challenge. In particular, the eddy covariance (EC) method, which is widely used for measuring fluxes of energy and gasses between the surface and atmosphere, consistently produces greater incoming than outgoing energy flux measurements (Foken, 2008, Mauder et al., 2020). This imbalance indicates that there is bias in one or more of the measured fluxes or that typically neglected fluxes contribute significantly to the overall energy budget.

## 1.1 Surface-atmosphere energy budget

The major components of the surface-atmosphere energy budget include net radiation ( $R_n$ ), ground heat flux ( $G$ ), sensible heat flux ( $H$ ) and latent heat flux ( $\lambda E$ ). The first law of thermodynamics dictates that the energy fluxes into the surface should be exactly balanced by outgoing energy fluxes. This can be expressed as:

$$R_n - G = H + \lambda E \quad (1.1)$$

Where a positive  $R_n$  value corresponds to energy absorbed at the surface while positive values of  $G$ ,  $H$ , and  $\lambda E$  represent energy fluxes away from the surface.  $H$  and  $\lambda E$  technically represent the fluxes of sensible and latent heat directly at the surface-atmosphere interface. However, they are typically assumed to be equivalent to the turbulent fluxes measured by an EC system at some distance above the canopy. The turbulent fluxes are calculated as follows:

$$H = \rho c_p \overline{w'T'}, \quad \lambda E = \lambda \rho \overline{w'q'} \quad (1.2)$$

Where  $w$ ,  $T$ , and  $q$ , represent vertical wind velocity, air temperature and water vapor mixing ratio, respectively.  $\rho$ ,  $c_p$ , and  $\lambda$  are, respectively, the air density, specific heat capacity of air, and latent heat of vaporization of water. Overbars represent temporal

means over a chosen averaging period and primes denote deviations from the temporal mean.

The sum of the terms of the left-hand side of Equation 1.1 are often referred to as available energy. In the case of energy balance non-closure, the energy balance residual or imbalance ( $Imb$ ), is defined as the difference between the available energy and the sensible and latent heat fluxes, as given in Equation 1.3:

$$Imb = R_n - G - H - \lambda E \quad (1.3)$$

Figure 1.1 shows the average diel cycle of each of the terms of in Equation 1.3 measured during the CHEESEHEAD19 experiment, the dataset used in this study.

## 1.2 Issues affecting energy balance closure

Energy balance non-closure is a well-established problem across most flux sites. The mean imbalance is typically positive in sign and represents between 10% and 30% of the measured available energy (Foken, 2008, Oncley et al., 2007, Twine et al., 2000, Wilson et al., 2002). Many potential sources of this error have been proposed and investigated. These broadly fall under two categories: 1) errors associated with data collection and processing, and 2) contributions by typically neglected energy budget components (Leuning et al., 2012, Mauder et al., 2020).

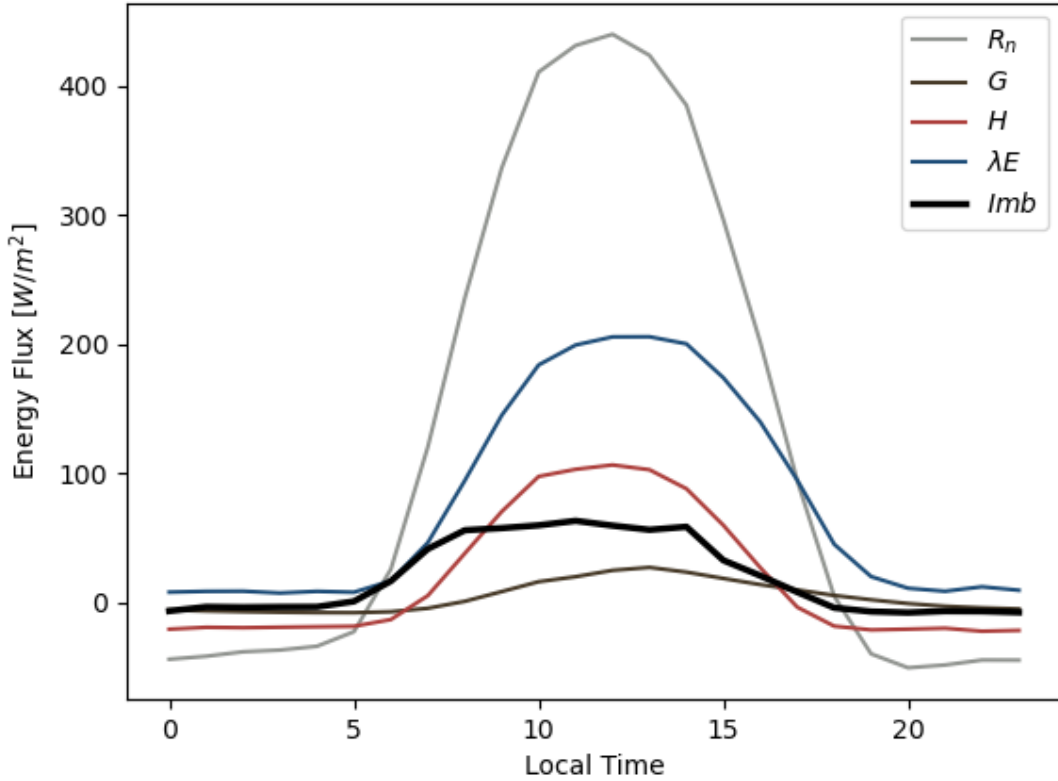


FIGURE 1.1: Diel cycle of measured energy balance components from the CHEESE-HEAD19 dataset. Values are average across all days and measurement sites.

### 1.2.1 Data collection and processing errors

Errors introduced through instrumentation and data processing can have a significant impact on energy balance closure (Mauder et al., 2007). It has generally been ruled out, however, that any of these issues are responsible for the consistent under-closure of the energy balance. This is largely because most errors in this category are random and thus should not contribute to a systematic measurement bias (Mauder et al., 2020). Several data processing steps and corrections have been introduced which, when implemented

carefully, tend to reduce the energy balance residual (Mauder and Foken, 2006). These include a correction for frequency response losses presented by Moore (1986) as well as the Webb et al. (1980) correction for density changes due to temperature and water vapor. These corrections have generally become standard procedures in EC data processing (Foken, 2008).

One notable instrumentation issue that continues to affect many flux sites is related to the differing footprints of the instruments used to measure each component of the energy balance equation. The eddy covariance system measures turbulent fluxes on a length scale of roughly 100 m or more, depending on tower height. The measurement scales of the net radiation and ground heat flux sensors, however, are on the order 10 and 0.1 m, respectively (Mauder et al., 2020). Unless a site has a highly homogeneous land cover,  $R_n$  and  $G$  measurements may not be representative of the area from which the turbulent fluxes are measured, possibly contributing to energy imbalance (Lee and Black, 1993). This issue can be mitigated by carefully selecting the location of  $R_n$  and  $G$  sensors to maximize representativeness or using multiple sensors to sample the heterogeneity of the turbulent flux footprints (Schmid, 1997).

Another source of error in EC measurements which can be categorized under data processing issues is that of the averaging time. The EC method relies on the assumption that the mean vertical wind velocity over the chosen averaging period is negligible (Moncrieff et al., 1997). The averaging period acts as a high pass filter such that transport by way of eddies with time scales larger than the averaging time are not included in the eddy

flux. It is thus necessary to choose a time period long enough to capture the majority of the eddies responsible for transport of the scalar of interest, yet short enough that the bulk properties of the boundary layer remain relatively unchanged (Metzger and Holmes, 2007). It has been established by way of the Ogive method that a 30 minute averaging period is typically the optimal length to fulfill both of these criteria (Mauder et al., 2020). However, some studies have suggested that longer averaging periods could improve energy balance closure (Finnigan et al., 2003, Foken et al., 2006). On the other hand, Lee and Black (1993) found that increasing the averaging period beyond 30 minutes did not significantly reduce the energy imbalance.

### 1.2.2 Additional energy fluxes

In addition to the assumption of negligible mean vertical velocity, the eddy covariance method is intended to be used over a horizontally homogeneous surface (Finnigan et al., 2003). Further, it is assumed that there is a constant flux layer above the canopy such that the flux divergence between the canopy and measurement point is negligible (Foken and Wichura, 1996). Under such conditions, turbulent fluxes measured from a tower above the canopy, would constitute the entirety of the scalar flux from the surface. However, many real-world measurement sites violate one or more of these assumptions. In such cases, a more rigorous, three-dimensional approach is often necessary in order to accurately characterize the surface energy budget (Baldocchi, 2003). Equation 1.4 describes the net surface atmosphere exchange (NSAE) of a conserved tracer within a control volume centered on a flux tower, as presented in Metzger (2018).

$NSAE =$

$$\int_0^{z_m} \left[ \frac{1}{4l^2} \int_{-l}^l \int_{-l}^l \frac{\partial \bar{c}}{\partial t} dx dy \right] dz \quad (\text{I})$$

$$\int_0^{z_m} \left[ \frac{1}{4l^2} \int_{-l}^l \int_{-l}^l \left\{ \frac{\partial \bar{u}c}{\partial x} + \frac{\partial \bar{u}'c'}{\partial x} + \frac{\partial \bar{v}c}{\partial y} + \frac{\partial \bar{v}'c'}{\partial y} \right\} dx dy \right] dz \quad (\text{II})$$

$$\int_0^{z_m} \left[ \frac{1}{4l^2} \int_{-l}^l \int_{-l}^l \left\{ \frac{\partial \bar{w}c}{\partial z} + \frac{\partial \bar{w}'c'}{\partial z} \right\} dx dy \right] dz \quad (\text{III})$$

(1.4)

Where  $c$  is a tracer value such as temperature or water vapor mixing ratio.  $u$ ,  $v$ , and  $w$  represent wind velocity in the  $x$ ,  $y$ , and  $z$  directions, respectively.  $2l$  and  $z_m$  are, respectively, the side length and height of a square-based control volume. The top of the control volume is parallel with the surface and incident with the EC measurement point. The three lines on the right-hand side of Equation 1.4 represents the following with respect to tracer  $c$ : Line I) storage within the control volume, Line II) horizontal flux through the sides of the control volume, Line III) vertical flux through the top of the control volume.

If it is assumed that the control volume is horizontally homogeneous, or that the measurements taken at the tower are representative of the horizontal plane of the control volume in which they were taken, the horizontal integration is not needed. Additionally, horizontal flux divergence, the second and fourth terms in line II, are typically assumed to be negligible (Lee, 1998).

These simplifications lead to the following:

$$NSAE = \int_0^{z_m} \left[ \frac{\partial \bar{c}}{\partial t} + \frac{\partial \bar{u}\bar{c}}{\partial x} + \frac{\partial \bar{v}\bar{c}}{\partial y} + \frac{\partial \bar{w}\bar{c}}{\partial z} + \frac{\partial \overline{w'c'}}{\partial z} \right] dz \quad (1.5)$$

The second and third terms on the right hand side of Equation 1.5 can be expanded and rewritten as follows,

$$\frac{\partial \bar{u}\bar{c}}{\partial x} + \frac{\partial \bar{v}\bar{c}}{\partial y} = \bar{u} \frac{\partial \bar{c}}{\partial x} + \bar{c} \frac{\partial \bar{u}}{\partial x} + \bar{v} \frac{\partial \bar{c}}{\partial y} + \bar{c} \frac{\partial \bar{v}}{\partial y} = \bar{u} \frac{\partial \bar{c}}{\partial x} + \bar{v} \frac{\partial \bar{c}}{\partial y} - \bar{c} \frac{\partial \bar{w}}{\partial z} \quad (1.6)$$

Because for non-divergent flow,

$$\frac{\partial \bar{u}}{\partial x} + \frac{\partial \bar{v}}{\partial y} = -\frac{\partial \bar{w}}{\partial z} \quad (1.7)$$

If the coordinate system is set such that the mean wind is in the x direction,  $\bar{v} = 0$ . This leaves:

$$NSAE = \int_0^{z_m} \left[ \frac{\partial \bar{c}}{\partial t} + \bar{u} \frac{\partial \bar{c}}{\partial x} + \frac{\partial \bar{w}\bar{c}}{\partial z} - \bar{c} \frac{\partial \bar{w}}{\partial z} + \frac{\partial \overline{w'c'}}{\partial z} \right] dz \quad (1.8)$$

Additionally under the assumption of a linear vertical wind profile,

$$\frac{\partial \bar{w}}{\partial z} = \frac{\bar{w}(z_m)}{z_m} \quad (1.9)$$

This substitution can be made in the fourth term on the right hand side of Equation 1.8. Finally, the last three terms can be integrated and simplified assuming zero vertical wind at the surface ( $w(0) = w'(0) = 0$ ), resulting in:

$$NSAE = \int_0^{z_m} \frac{\partial \bar{c}}{\partial t} dz + \int_0^{z_m} \bar{u} \frac{\partial \bar{c}}{\partial x} dz + \bar{w}(z_m)(\bar{c}(z_m) - \langle c \rangle) + \overline{w'c'}(z_m) \quad (1.10)$$

Where  $\langle c \rangle$  denotes the vertically-averaged value of  $c$ . The remaining terms constitute the following 1) storage 2) horizontal advection 3) vertical advection, and 4) vertical turbulent flux at the top of the control volume, as is typically measured by EC systems. Measuring terms 1-3 requires additional instrumentation beyond a standard EC setup. This added cost, as well as the understanding that these terms should disappear under ideal conditions, has led to the common practice of neglecting them (Finnigan et al., 2003). Though the storage term is often measured at sites with tall canopies. Despite their insignificance under ideal conditions, the systematic EC energy imbalance is often attributed to one or more of these terms, indicating that they must be quantified in order to fully characterize surface-atmosphere energy exchange (Leuning et al., 2012, Massman and Lee, 2002).

### 1.2.2.1 Storage

Of these additional terms, energy storage in the air is the most easily, and frequently, quantified. This can be done using profile measurements of temperature and humidity taken on the flux tower (Xu et al., 2019). In addition to storage of sensible and latent heat in the air, thermal energy can also be stored in the vegetation (biomass storage), as well as in the soil between the surface and the ground heat flux measurement plate. These components can be quantified through additional temperature measurements, as well as estimates of the heat capacity and density of soil and biomass (Lindroth et al., 2010). The storage term averages to near zero on a daily or annual basis (Leuning et al., 2012), and thus cannot explain the pattern of positive mean energy imbalance. However, inclusion of these terms has been shown to improve energy budget closure for half-hour measurement periods (Haverd et al., 2007, Leuning et al., 2012, Lindroth et al., 2010). When storage terms are quantified, they are often included with the available energy (the left hand side of Equation 1.3) to indicate that this energy does not contribute to the surface-atmosphere fluxes.

Energy can also be stored in the vegetation in the form of chemical energy by way of photosynthesis. Meyers (2004), Oncley et al. (2007), and Xu et al. (2017) each estimated energy storage by photosynthesis in crop canopies and found that photosynthetic energy uptake comprised a few percent of the net radiation. Thus, accounting for this flux marginally improves energy balance closure but is not sufficient to fully address the

imbalance.

### 1.2.2.2 Horizontal Advection

Horizontal advection is the product of the mean horizontal wind and the horizontal gradient of a scalar,  $c$  (term 2 on the right-hand side of Equation 1.10). This term disappears if the mean horizontal wind is zero, a rare occurrence, or under the condition of horizontal homogeneity. While horizontal homogeneity is a common assumption, and selection criteria for flux sites, some degree of heterogeneity is inevitable. Even if the entire flux tower footprint is contained within a highly homogeneous area, horizontal advection can occur due to a surface change well upwind of the tower (Higgins et al., 2013, Wang et al., 2024).

Horizontal advective fluxes cannot be measured using a single flux tower alone. Some studies have attempted to quantify horizontal advection using two or more measurement points aligned parallel to the predominant wind (Kochendorfer and Paw U, 2011, Wang et al., 2024). Others have used multiple towers in order to be able to calculate horizontal gradients regardless of wind direction (Moderow et al., 2007, 2021, Morrison et al., 2021, 2023). Higgins et al. (2013) used lidar measurements of wind and water vapor to estimate latent heat advection while Cuxart et al. (2016) and Garcia-Santos et al. (2019) both used remotely sensed land surface temperature (LST) to calculate horizontal advection of sensible heat. Higgins et al. (2013), Kochendorfer and Paw U (2011), Morrison et al. (2023), and Wang et al. (2024) all demonstrated improved energy balance closure with

the inclusion of horizontal advective fluxes. Cuxart et al. (2016) and Garcia-Santos et al. (2019) investigated the relative contribution of horizontal advection driven by different scales of surface heterogeneity. Both studies found that heterogeneities on the hectometer scale resulted in horizontal advective fluxes with values on the order of the energy residual, while horizontal advection due to kilometer scale heterogeneity was much smaller.

### 1.2.2.3 Vertical Advection

While the lack of horizontal tracer gradients is typically the justification for ignoring horizontal advection, it is the assumption of relatively insignificant mean vertical wind velocity ( $\bar{w} \ll \sigma(w')$ , where  $\sigma$  represents the standard deviation) that allows for the neglect of vertical advection. This is a standard assumption in EC flux measurements. However, non-zero  $\bar{w}$  values regularly occur and can lead to non-negligible vertical advective fluxes (Lee, 1998, Lee and Black, 1993). As an example, a few hours of vertical velocity measurements from the CHEESEHEAD19 dataset are shown in Figure 1.2. In this figure, the raw 20 Hz vertical wind velocity ( $w = \bar{w} + w'$ ) values are shown alongside the 30-minute average  $\bar{w}$ . It can be seen that while magnitudes of  $\bar{w}$  are much smaller than fluctuations in the 20 Hz data, non-zero  $\bar{w}$  values do occur, indicating the possibility of for advective fluxes.

Vertical advection can occur over sloping terrain or tall vegetation where the wind streamlines at the top of a flux tower can diverge from parallel to the surface, resulting in a

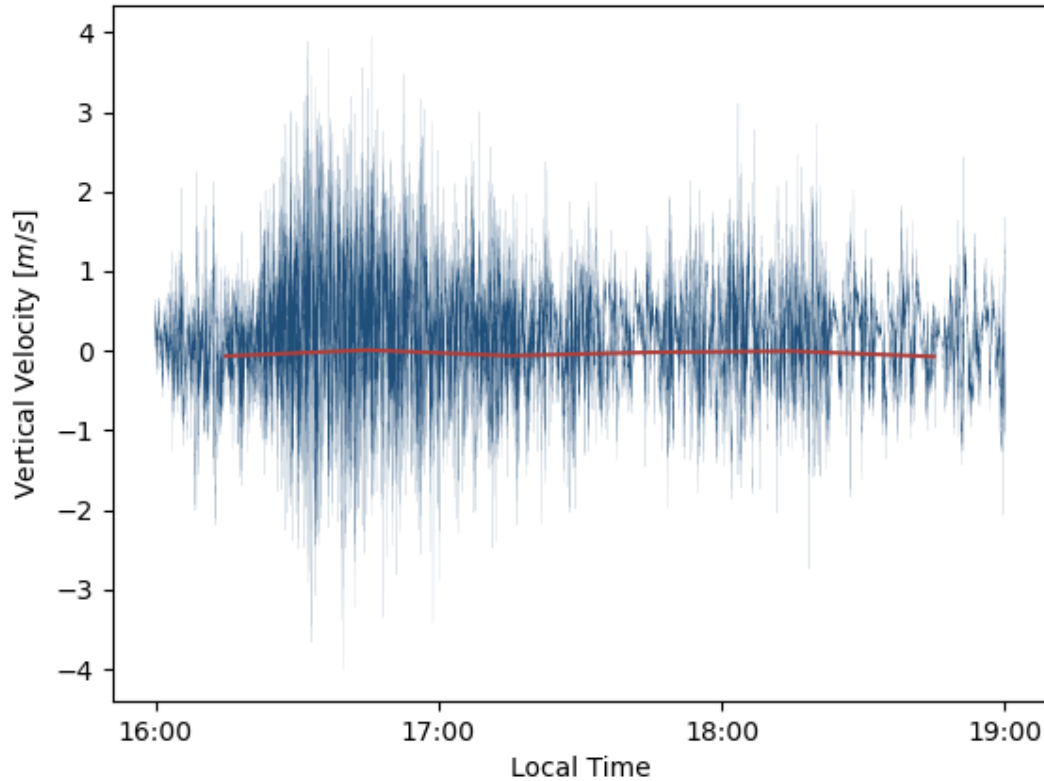


FIGURE 1.2: Time series of vertical wind velocity from 16:00-19:00 local time on August 20, 2019 at NE1 tower. 20 Hz measurements are shown in blue with the 30 minute average in red.

finite vertical velocity (Finnigan and Brunet, 1995, Lee, 1998, Lee and Hu, 2002). Alternatively, large-scale atmospheric motions called secondary circulations (SCs) can result in substantial, non-zero  $\bar{w}$  values over the EC averaging period. One type of SC moves with the mean horizontal wind but is large enough such that its transit time past the measurement point is greater than the averaging time. As a result, the EC system is unable to sufficiently sample the vertical velocity, resulting in a finite  $\bar{w}$  (Eder and Mauder, 2015, Inagaki et al., 2006, Kanda et al., 2004). A second type of SC is driven by differences in

surface heating that cause updrafts in some areas and downdrafts in others. These SCs typically do not move horizontally and, as a result, a flux tower may only measure an updraft or the downdraft throughout the life of the SC (Foken, 2008, Inagaki et al., 2006, Mauder et al., 2010).

Vertical advection of a scalar,  $c$ , can be measured from a single tower with profile measurements of  $c$  and vertical velocity measured by a sonic anemometer. A number of studies have used this method to quantify vertical advection of energy (Kochendorfer and Paw U, 2011, Moderow et al., 2007, Morrison et al., 2021, Wanner et al., 2024) or CO<sub>2</sub> (Aubinet et al., 2005, Feigenwinter et al., 2008, Novick et al., 2014). While vertical advective fluxes are often found to be large enough to suggest that they should be accounted for, the measurements often suffer from a high degree of scatter (Feigenwinter et al., 2008, Moderow et al., 2007, Wang et al., 2024), particularly over more heterogeneous sites (Morrison et al., 2021). This issue is typically attributed to challenges in measuring the extremely small  $\overline{w}$  values that drive vertical advection. Error in these values can be caused by improper rotation of the sonic anemometer (Lee, 1998) or simply by lack of precision of the vertical wind measurements (Kochendorfer and Paw U, 2011).

As an alternative to directly calculating advective fluxes, spatial eddy covariance has been suggested as a way to capture the transport of scalars by way of SCs. In this method, anomalies of vertical wind and tracer values are calculated from a spatial mean, rather than a temporal mean (Mahrt et al., 1994, Steinfeld et al., 2007). Fluxes calculated by way of spatial EC can capture transport by secondary circulations that may not

be sufficiently sampled at one measurement point. However, it is necessary to have a sufficient density of measurements within that domain in order to sample both updrafts and downdrafts of the large-scale eddies (Steinfeld et al., 2007). The CHEESEHEAD19 dataset was previously used by Butterworth et al. (2024) to calculate spatial EC energy fluxes. This study was not able to improve energy balance closure by using spatial EC as compared to traditional temporal EC which they attribute in part to a need for a higher spatial density of measurements.

#### 1.2.2.4 Relationship between advective flux components

A number of studies have looked at horizontal and vertical advective fluxes in relation to each other. Some studies of CO<sub>2</sub> fluxes have found that horizontal and vertical fluxes are often of similar magnitude and opposite sign and thus partially offset each other (Aubinet et al., 2003, Yi, 2008). These findings, however, apply specifically to night time conditions in sloped terrain when the atmosphere is typically statically stable and friction velocity,  $u_*$  is low. Katul et al. (2006) also found, in a model of flow over hilly terrain, that horizontal and vertical CO<sub>2</sub> fluxes tend to be of opposite signs, though they do not often fully cancel each other out. It is unclear whether a similar pattern of opposite horizontal and vertical fluxes occurs for advective energy fluxes as well as CO<sub>2</sub>.

The relationship between the sensible and latent heat components of the advective fluxes is also of interest. In order to close the surface energy balance,  $Imb$  must be partitioned between sensible and latent heat fluxes. Twine et al. (2000) proposed a method that used

the Bowen ratio ( $B$ ), defined as  $H/\lambda E$ , from the measured turbulent fluxes to partition the energy imbalance. While this method is commonly used to close the energy budget, there is little evidence to support its accuracy. Eder et al. (2014) found that for  $B$  values close to 1, the total Bowen ratio was reasonably well-estimated by the Bowen ratio of the turbulent fluxes. For other  $B$  values, however, the latent heat flux was underestimated by partitioning the energy imbalance with the turbulent Bowen ratio.

### 1.2.3 Conditions associated with Energy Imbalance

Certain atmospheric and site conditions have been associated with greater energy imbalance, indicating that under such conditions storage and advective fluxes may contribute substantially to the surface energy budget. In particular, Barr et al. (2006), Franssen et al. (2010), Wilson et al. (2002), and Zhou and Li (2019) all found that energy imbalance increases under low  $u_*$  values, which correspond to conditions of weaker mechanical turbulent mixing. In addition, many studies have found a relationship between atmospheric stability and energy balance. Butterworth et al. (2024), Lindroth et al. (2010), Stoy et al. (2013), and Zhou and Li (2019) showed that energy balance closure decreases under increasingly unstable conditions. Others, however, found that energy balance improves as conditions transition from near neutral to strongly unstable (Mauder et al., 2010, McGloin et al., 2018). Under statically stable conditions, which most often occur at night,  $Imb$  is typically negative, indicating greater measured outgoing than incoming fluxes.  $Imb$  is typically smaller in magnitude but greater relative to the available energy at night than during the day (Franssen et al., 2010, Mauder et al., 2010).

In addition to atmospheric conditions, the degree of surface heterogeneity at a site has been consistently observed to be positively correlated with energy imbalance (Panin et al., 1998, Stoy et al., 2013, Xu et al., 2017). Heterogeneity can create horizontal gradients, allowing for horizontal advection (Cuxart et al., 2016), as well as drive secondary circulations which can result in vertical advection Desjardins et al. (1997), Kanda et al. (2004), Mahrt et al. (1994).

### 1.3 Research Objectives

While the connection between heterogeneity and energy balance is well documented, improving energy balance closure at heterogeneous sites remains a challenge. In this study, we use the dense network of measurements taken during the CHEESEHEAD19 experiment to quantify advective energy fluxes and assess their contribution to surface energy balance closure. The CHEESEHEAD19 experiment was conducted with the goal of better understanding the drivers of energy balance non-closure in a heterogeneous landscape (Butterworth et al., 2021). Here, we estimated the horizontal and vertical advective fluxes of sensible and latent heat in order to answer the following questions:

1. Can we derive reasonable estimates of advective fluxes from the tower measurements taken during the CHEESEHEAD19 campaign?
2. Are there relationships between the different components of the advective fluxes?

How do these compare to previously hypothesized or observed relationships?

- Do horizontal and vertical fluxes tend to partially offset each other?

- Is the Bowen ratio of the turbulent fluxes a reasonable estimate of the advective flux Bowen ratio?
3. How do environmental conditions such as time of day, season, and atmospheric stability impact the calculated advective fluxes and their contribution to energy balance closure?
  4. Is energy balance closure improved when advective fluxes are included?
  5. How sensitive are the calculated advective fluxes to variations in the method used to estimate them?

# Chapter 2

## Data and Methods

### 2.1 The CHEESEHEAD19 Experiment

The Chequamegon Heterogeneous Ecosystem Energy-balance Study Enabled by a High-density Extensive Array of Detectors, 2019 (CHEESEHEAD19) experiment was conducted in Northern Wisconsin between June and October of 2019. The study focused on a highly heterogeneous landscape consisting of both forested and aquatic surface types. The 10 km by 10 km study domain was centered on the Park Falls NOAA/Ameriflux tower (WLEF/US-PFa). 19 additional flux towers were deployed within the study domain in order to sufficiently sample the variation of surfaces and atmospheric processes across the landscape. Additional data was collected during the CHEESEHEAD19 field campaign, including airborne flux measurements and surveys of the vegetation. This

study, however, focuses on data collected at 18 of the 20 flux tower sites within the domain (NCAR/EOL In-situ Sensing Facility and Oncley, 2021). A detailed description of the CHEESEHEAD19 experiment can be found in Butterworth et al. (2021). Figure 2.1 is a map of the CHEESEHEAD domain showing the location of the flux towers included in this study.

## 2.2 Data Used

In the present study, we used measurements from the WLEF tower as well as 17 of the additional, temporary towers deployed during the CHEESEHEAD19 study period. Standard meteorological and EC measurements are taken at three levels on the WLEF tower: 30 m, 122 m, and 396 m above ground level (AGL). Only measurements taken at 30 m were used for this study. Each of the additional towers had between one and three measurement levels where air temperature ( $T$ ) and water vapor mixing ratio ( $q$ ) were measured.  $R_n$ , turbulent fluxes of  $H$  and  $\lambda E$ , and horizontal wind speed and direction were measured at the highest measurement level on each tower. Ground heat flux ( $G$ ), heat storage in soil ( $S_s$ ), as well as sensible and latent heat storage in air ( $S_H$  and  $S_{\lambda E}$ , respectively), were also measured.

The measurement levels of each of the towers are given in Table 2.1. These AGL heights were derived from precise above sea level (ASL) elevation measurements taken at each measurement level on the towers. ASL elevations of the tower bases were, however, not measured. This prevented us from directly calculating AGL measurement heights. In




---

FIGURE 2.1: Map of CHEESEHEAD19 tower locations. Coordinates are given in degrees E and degrees N.

order to estimate AGL heights, we took approximate heights of the lowest level, as given in CHEESEHEAD19 experiment documentation, and used the differences between ASL elevations summed with the approximate height of the lowest level to determine the heights of the higher levels.

Tower	Sensor level 1	Sensor level 2	Sensor level 3	Level 1 Elevation
WLEF	-	-	30	-
NW1	2	11.7	33.3	476.3
NW2	2	10.8	-	476.3
NW3	2	-	-	468.5
NW4	2	16.5*	32.7	476.7
NE1	2	11.9	33.4	495.2
NE2	2	11.9	33.3	482.6
NE3	2	12.1	33.5	490.1
NE4	2	11.5	32.5	484.7
SW1	2	12	33.5	471.3
SW2	2	11.9	28.5*	473.1
SW3	2	11.3	32.7	472.8
SW4	2	11.3	32.4	486.4
SE2	2	11.9	33	485.7
SE3	2	11.9	33.4	479.5
SE4	3	-	-	469.3
SE5	2	11	-	482.8
SE6	2	11.3	30.4*	483

TABLE 2.1: AGL Sensor heights for  $T$  and  $q$  measurements for each tower as well as ASL elevation for the lowest measurement level. All measurements in m. Values with asterisks indicate measurement levels that were too far from others to be treated as if in the same horizontal plane, as described in section 2.3.1

## 2.3 Advection Quantification

### 2.3.1 Horizontal Advection

The horizontal advective flux of  $T$  and  $q$ , as given in term II on the right-hand side of Equation 1.10, can be found by vertically integrating the product of horizontal wind speed,  $\bar{u}$ , and the horizontal gradient of  $T$  or  $q$ ,  $\partial c/\partial x$ . Here, we did this by numerically integrating the product of profiles of  $\bar{u}$  and  $\partial c/\partial x$  with a step size of 0.1 m. These fluxes of  $T$  and  $q$  can be converted to fluxes of  $H$  and  $\lambda E$  in the same way as the turbulent fluxes, as given in Equation 1.2.

Profiles of the horizontal wind as a function of height,  $z$ , were estimated using a logarithmic wind profile above the canopy and an exponential profile within the canopy. The basic logarithmic profile for wind speed at height  $z$  is:

$$\bar{u}(z) = u_* k \ln\left(\frac{z-d}{z_0}\right) \quad (2.1)$$

Where  $u_*$  is the friction velocity and  $k$  is the von Karman constant taken to be 0.4. The displacement height  $d$ , and roughness length,  $z_0$ , are assumed to be  $0.67z_m$  and  $0.1z_m$ , respectively. When  $\bar{u}$  was calculated at the top of the tower,  $z_m$ , using this equation with measured  $u_*$  values,  $\bar{u}(z_m)$  was found to frequently differ from the measured wind speed by more than 100%. Rather than using the measured  $u_*$  to calculate wind profiles, an effective  $u_*$  value was backed out of 2.1 by substituting in the measured  $\bar{u}(z_m)$  value.

The exponential wind profile presented in Inoue (1963) was used to calculate  $\bar{u}$  within the canopy.

$$\bar{u}(z) = \bar{u}(h) \exp\left[a\left(\frac{z}{h} - 1\right)\right] \quad (2.2)$$

The VIIRS Leaf Area Index (LAI) product (Myneni, 2023) was used to parameterize the attenuation coefficient  $a$  as  $LAI/2$  (Yi, 2008). This in-canopy profile model is valid for canopies with uniform leaf area density ( $LAD$ ) which is an oversimplification for most forest canopies. However,  $LAD$  was not measured during the CHEESHEAD19

experiment, preventing the use of more complex models that account for non-uniform *LAD*.

In the lowest part of the canopy, where  $z < z_0$ , a second logarithmic profile was used in which the displacement height was taken to be 0 and the roughness length representative of the underlying surface rather than the vegetation, as denoted by a subscript *s*, was used (Campbell and Norman, 1998). The full profile, with the  $u_*$  modification can be written as,

$$\bar{u}(z) = \begin{cases} \frac{\bar{u}(z_m)}{\ln\left(\frac{z_m-d}{z_0}\right)} \times \ln\left(\frac{z-d}{z_0}\right) & \text{if } z \geq h \\ \bar{u}(h) \exp\left[a\left(\frac{z}{h} - 1\right)\right] & \text{if } z < h \\ \frac{\bar{u}(z_0)}{\ln\left(\frac{z_0}{z_{0,s}}\right)} \times \ln\left(\frac{z}{z_{0,s}}\right) & \text{if } z < 0.1h \end{cases} \quad (2.3)$$

An interpolation method was used to calculate the horizontal gradients of  $T$  and  $q$ . The interpolation was carried out across three horizontal planes, corresponding to the three measurement heights at most of the towers, to produce profiles of  $T$  and  $q$  at points 1 km upwind and downwind of each tower as shown in Figure 2.2. This distance was chosen based on a scale analysis of the size of eddies that are unaccounted for in the EC fluxes. An eddy moving at 1 m/s will travel 1800 m over the 30-minute averaging period. Thus we predicted that it would be possible to estimate the horizontal gradients within large eddies that are not captured by the EC fluxes by using points located 2 km apart. The interpolation was executed using `scipy RBFInterpolator` with the default thin plate spline

kernel. The locations of the upwind and downwind points for each tower were determined using the wind direction measured at the top of the tower.

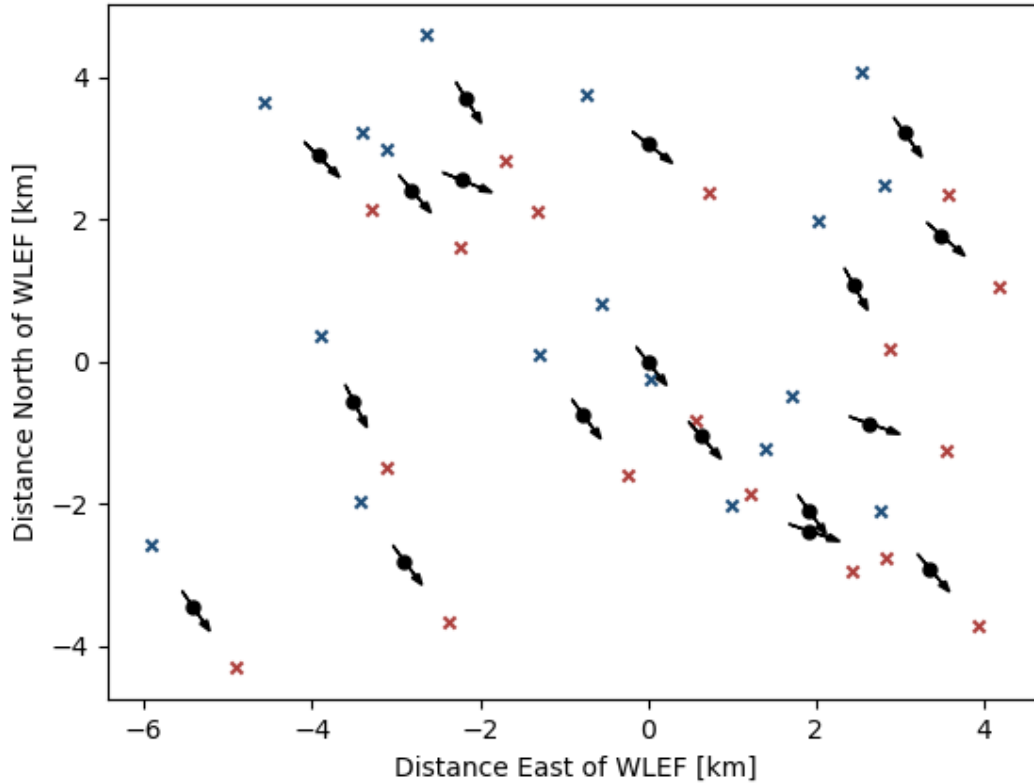


FIGURE 2.2: Map of CHEESEHEAD19 domain showing horizontal interpolation method and wind directions. Black dots mark the flux towers where  $T$  and  $q$  were directly measured. Arrows show the wind direction measured at each tower. Xs mark the upwind (blue) and downwind (red) points to which  $T$  and  $q$  were interpolated.

Most of the measurement heights were within 1 m of 2 m, 11.5 m, or 33 m AGL, the nominal measurement heights for each level. Measurements within each of these groups were treated as being representative of the same horizontal plane. In the case of towers NW4, SW2, and SE6 where measurements were taken well above or below the nominal measurement heights,  $T$  and  $q$  were linearly interpolated or extrapolated to the height of

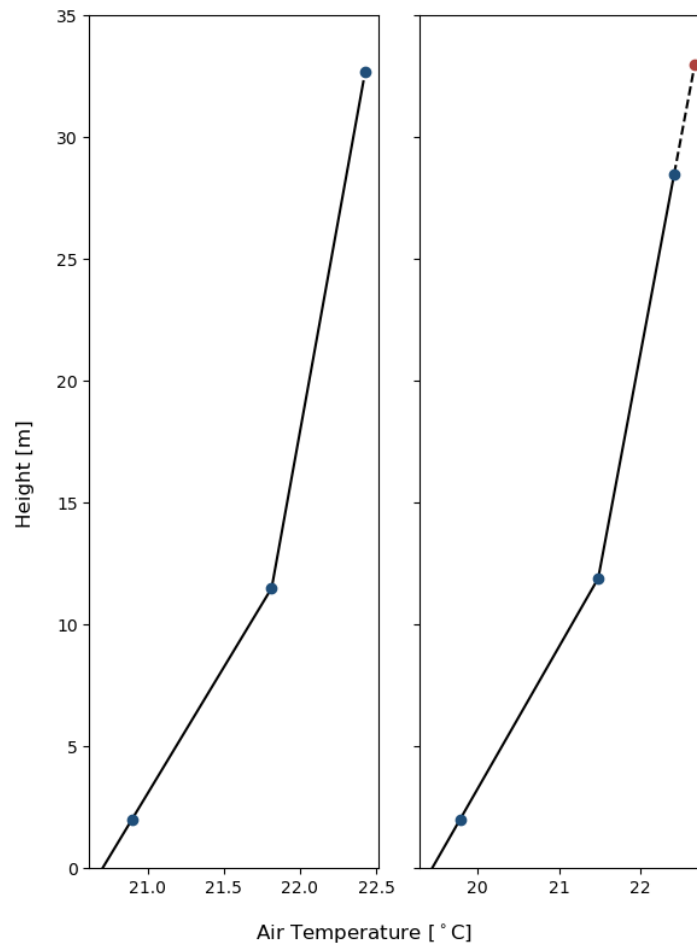
the horizontal interpolation plane as shown in Figure 2.3. Since only one measurement height was available for the WLEF tower, it was not possible to extrapolate the  $T$  and  $q$  measurements to 33 m for that tower. Instead the 30 m measurement was included with the 33 m measurements from other towers.

Vertical profiles of  $c$  at the upwind and downwind locations were then determined by assuming a linear profile between interpolated values and extending the slope between the lowest two measurements to the surface as shown in Figure 2.3. Profiles of  $\partial c/\partial x$  were calculated by taking the differences between downwind and upwind profiles divided by the distance between the downwind and upwind points as given in Equation 2.4.

$$\frac{\partial c}{\partial x} = \frac{c_{downwind} - c_{upwind}}{\Delta x} \quad (2.4)$$

### 2.3.2 Vertical Advection

The vertical advective fluxes were calculated according to the third term in Equation 1.10.  $\bar{w}$  was found by averaging the geographically-corrected sonic anemometer vertical velocity measurements over each 30-minute time interval. The vertically averaged  $T$  and  $q$  values,  $\langle \bar{c} \rangle$ , were found by averaging vertical profiles determined in the same way as the upwind and downwind profiles for the horizontal advection term. In this case, measurements at the towers were used, rather than interpolated values upwind and downwind of the towers. This method is in line with a number of other studies that investigated vertical advection including Moderow et al. (2021). For towers with only one measurement height, there



---

FIGURE 2.3: Left: Example vertical profile of  $T$  at the NW1 tower determined by linearly interpolating measurements taken at the point marked by blue dots. Right: Profile from SW2 tower showing that  $T$  was linearly extrapolated to 33 m for use in the horizontal interpolation. Both profiles from 18:00 local time on July 20, 2019.

was not enough information to calculate vertical gradients. Only horizontal advection was calculated for these towers. As a result, they are excluded from some of the following analyses.

## 2.4 Energy Balance Analysis

In order to assess the contribution of the advective energy fluxes to the overall energy balance closure, the energy imbalance was calculated with ( $Imb_A$ ) and without ( $Imb_{NA}$ ) the advective terms. Equation 2.5 was used to calculate  $Imb_A$ .

$$Imb_A = R_n - G - H_{turb} - LE_{turb} - S_s - S_H - S_{\lambda E} - H_{HA} - \lambda E_{HA} - H_{VA} - \lambda E_{VA} \quad (2.5)$$

Where the first four terms on the right-hand side are the same as those presented in equation 3.  $S_s$  is the soil heat storage term while  $S_H$  and  $S_{\lambda E}$  are the storage of sensible and latent heat in the air. The final four terms are the horizontal and vertical advection of sensible and latent heat with horizontal and vertical advection denoted by subscripts  $HA$  and  $VA$ , respectively.  $Imb_{NA}$  was calculated in the same way but without the advective terms.

The energy balance improvement ( $EBI$ ), due to the advective fluxes, was calculated as follows:

$$EBI = \frac{|Imb_{NA}| - |Imb_A|}{|Imb_{NA}|} \times 100\% \quad (2.6)$$

$EBI$  is positive if the magnitude of  $Imb$  is lower when the advective fluxes are included than without them, and negative if the opposite is true. This applies both for positive and negative residuals and if the residual changes sign with the inclusion of the advective fluxes. In some results presented below, however, only time periods with positive  $Imb_{NA}$  are included. The  $EBI$  was calculated from hourly  $Imb_{NA}$  and  $Imb_A$  values. Each site-hour was categorized as the energy balance having been improved, changed marginally, or made worse by the inclusion of the advective energy fluxes. These designations correspond respectively to  $EBI > 10\%$ ,  $-10\% \leq EBI \leq 10\%$ , and  $EBI < -10\%$ .

## 2.5 Case Evaluation

It is evident in a time series of the energy imbalance and total advective flux for a given tower that there are periods when these variables are closely aligned and other times when they appear to have a negative correlation. In order to investigate this phenomenon, we selected two nearly consecutive 24 hour periods of data from the NE1 tower. Period 1 (P1), from 17:00 on August 29 to 17:00 on August 30, was selected for its positive correlation between  $Imb_{NA}$  and total advection. During Period 2 (P2), from 08:00 on August 31 to 08:00 on September 1, on the other hand, total advection and  $Imb_{NA}$  appear to have reversed patterns. Total advection and  $Imb_{NA}$  for both periods are shown in Figure 2.4. These periods, selected for the apparent strong relationships between total advection and  $Imb_{NA}$ , were not intended to be representative of overall patterns in the dataset. However, similar periods of positive and negative correlation do somewhat regularly occur throughout the study for several of the towers. While P1 at

NE1 is not representative of the typical contribution of the calculated advective energy fluxes to the energy balance closure, the high correlation may indicate better accuracy in the estimated fluxes than at other times. As a result, this period may be useful in assessing relationships between true advective fluxes and other variables.

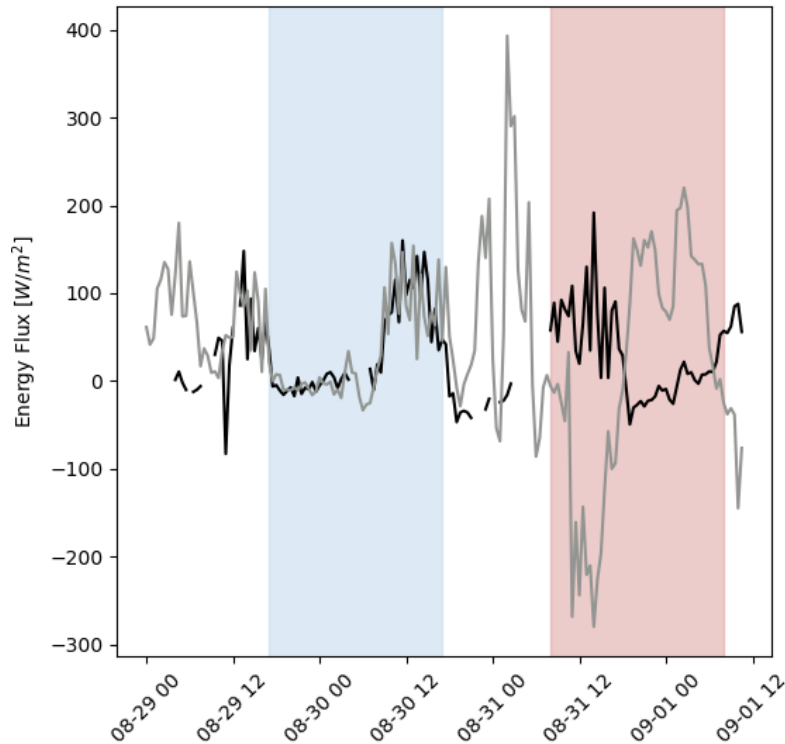


FIGURE 2.4: Time series of total advective energy flux (gray) and energy imbalance (black), showing the two case evaluation periods: P1 in blue and P2 in red.

## 2.6 Sensitivity Analysis

In order to assess the sensitivity of the calculated advective fluxes to methodological choices, a number of variations to the calculations were tested, as depicted in Figure 2.5.

Each of these variations is described in more detail below.

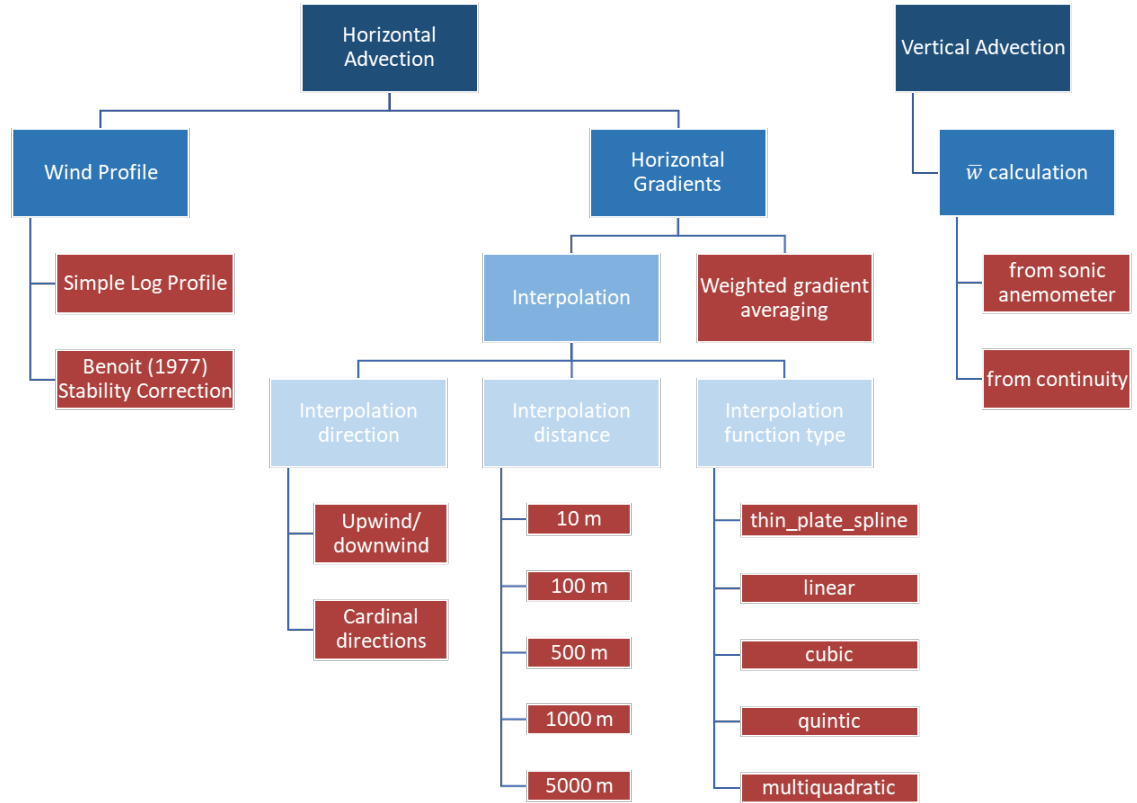


FIGURE 2.5: Decision tree diagram of calculation variation used in sensitivity analysis.

### 2.6.1 Wind Profiles

Equation 2.1 is technically only valid for statically neutral conditions (Stull, 1988). A correction factor,  $\Psi_M$  can be incorporated into the wind profile model as follows,

$$\bar{u}(z) = u_* k \left[ \ln\left(\frac{z-d}{z_0}\right) + \Psi_M \right] \text{ if } z \geq h \quad (2.7)$$

Benoit (1977) introduced the following formula for  $\Psi_M$ ,

$$\Psi_M = \ln \left[ \frac{(x_0^2 + 1)(x_0 + 1)^2}{(x^2 + 1)(x + 1)^2} \right] + 2 \tan^{-1}(x) - \tan^{-1}(x_0) \quad (2.8)$$

Where,

$$x = \left[ 1 - \left( \frac{15z}{L} \right) \right]^{1/4}, \quad x_0 = \left[ 1 - \left( \frac{15z_0}{L} \right) \right]^{1/4} \quad (2.9)$$

$L$  represents the Monin-Obukhov length. This correction was applied under unstable conditions, defined by  $L < 0$ .

## 2.6.2 Horizontal Gradients

### 2.6.2.1 Horizontal Interpolation Variations

In calculating horizontal gradients by way of horizontal interpolation, three different types of variations were considered. The first is the distance of the interpolation points from the towers. As described above, an interpolation distance of 1 km was used in the main analysis, chosen to represent the approximate scale of SCs that are expected to contribute to advective fluxes. However, as previously discussed, some studies have indicated that the scale of heterogeneity that matters most for horizontal advection is on the scale of hectometers (Cuxart et al., 2016, Garcia-Santos et al., 2019). In an attempt to test this, we varied the interpolation distance from 10 m to 5 km.

Additionally, the direction from the tower in which the interpolation points were located was varied. In the main analysis presented above, the interpolation points were located up and downwind of the tower and thus changed location as the wind shifted. The alternative tested here was to always interpolate to points in the cardinal directions from each tower. In this case, the wind vector was decomposed into north-south and east-west components. This may be a way to eliminate the location of the interpolation points relative to other towers as a confounding variable when assessing the impact of wind direction on advective fluxes.

The third variation tested was the type of function used in the interpolation. Of the `scipy RBFinterpolator` kernel options, “thin\_plate\_spline”, “linear”, “cubic”, “quintic”, and “multiquadratic” were tested.

### 2.6.2.2 Gradient Averaging Method

In addition to the interpolation method and variations described above, horizontal gradients of  $T$  and  $q$  were also estimated using a gradient averaging method. For each tower, gradients were calculated between that tower and every other tower within the domain. Given that the line connecting two towers is typically not parallel to the wind, gradients must be rotated or decomposed into  $x$  and  $y$  components in order to calculate advective fluxes. In order to do this, it was assumed that for each pair of towers, offsets between the towers in both the  $x$  and  $y$  directions contributed equally to the difference in  $T$  and  $q$  measurements. If the  $x$  axis is aligned with the mean wind, only the gradient in the  $x$

direction contributes to horizontal advection and the gradient in the  $y$  direction can be ignored. The  $x$  gradient between any two towers was thus estimated as

$$\frac{\partial c}{\partial x} \approx \frac{\Delta c \Delta x}{|\Delta x| + |\Delta y|} \quad (2.10)$$

Where  $\Delta c$  represented the difference in  $c$  value measured between the two towers and  $\Delta x$  and  $\Delta y$  are the distances between the towers in the  $x$  and  $y$  directions. For a given tower, a weighted average of  $\partial c/\partial x$  between that tower and every other tower was used to estimate the gradient across the main tower. The weighting factor is the inverse of the distance between the two towers such that,

$$\frac{\partial c}{\partial x} \approx \frac{1}{N} \times \sum_{i=1}^N (\Delta x_i^2 + \Delta y_i^2) \times \sum_{i=1}^N \left( \frac{\Delta c_i \Delta x_i}{|\Delta x_i| + |\Delta y_i|} \times \frac{1}{\Delta x_i^2 + \Delta y_i^2} \right) \quad (2.11)$$

The subscript  $i$  denotes each of the secondary towers that the main tower is paired with and  $N$  represents the total number of secondary towers. These gradients were calculated at the same 3 levels used in the horizontal interpolation method. The horizontal gradients at each tower were then linearly interpolated in the vertical to create profiles of  $\partial c/\partial x$  between the surface and measurement height.

### 2.6.3 Vertical Velocity Estimates

In the main analysis described above, averaged  $\bar{w}$  measurements from the sonic anemometer were used in the vertical advection calculations. Vertical velocity measured this way has been known to suffer from significant scatter (Feigenwinter et al., 2008, Moderow et al., 2007, Wang et al., 2024). As a comparison, vertical wind was also calculated from horizontal wind measurements and the continuity equation. Equation 1.7 describes the continuity of air under the assumption of incompressible flow. By integrating from the surface to the measurement height and applying the boundary condition  $\bar{w}(0) = 0$ , the vertical velocity at height  $z_m$  can be found as,

$$\bar{w}(z_m) = - \int_0^{z_m} \left[ \frac{\partial \bar{u}}{\partial x} + \frac{\partial \bar{v}}{\partial y} \right] dz \quad (2.12)$$

Here, the  $x$  and  $y$  axes are oriented in the west-east and south-north directions, respectively since the direction of the mean wind is different at each tower, preventing the use of a wind-parallel coordinate system. The horizontal gradients,  $\partial \bar{u} / \partial x$  and  $\partial \bar{v} / \partial y$  were found using a similar method as the horizontal gradients of  $T$  and  $q$ . First the wind profile model described in Equation 2.3, was used to calculate wind speed at 33 m AGL for all towers. This was decomposed in the  $\bar{u}$  and  $\bar{v}$  components.  $\bar{u}$  values were then interpolated to the east and west of each tower while  $\bar{v}$  was interpolated to the north and south. An interpolation distance of 1 km and the thin plate spline kernel were used. Horizontal gradients,  $\partial \bar{u} / \partial x(33 \text{ m})$  and  $\partial \bar{v} / \partial y(33 \text{ m})$ , were calculated across each tower. The

wind profile model (Equation 2.3) was then used to calculate profiles of gradients up to the measurement height for each tower. This is mathematically equivalent to calculating profiles of wind speed at each of the interpolation points and then taking the difference to find the profiles of gradients. These gradient profiles were then numerically integrated in accordance with Equation 2.12 to get  $\bar{w}(z_m)$ .

Advective energy fluxes were calculated using every possible combination of the above variations. This resulted in 102 different estimates of horizontal advective fluxes and 2 different estimates of vertical advection for a total of 204 possible estimates of total advection. The effect of each of the variations on the advective fluxes was assessed individually. Table 2.2 gives the cases that were used for this analysis. A complete list of all cases tested is presented in Table A.1.

Case	Horizontal Gradient Method	Interpolation Distance [m]	Interpolation Direction	Interpolation Kernel	Stability Correction
A	Interpolation	1000	Upwind downwind	thin_plate_spline	None
B	Interpolation	1000	Upwind downwind	thin_plate_spline	Benoit (1977)*
C	Interpolation	1000	NSEW*	thin_plate_spline	None
D	Interpolation	10*	Upwind downwind	thin_plate_spline	None
E	Interpolation	100*	Upwind downwind	thin_plate_spline	None
F	Interpolation	500*	Upwind downwind	thin_plate_spline	None
G	Interpolation	5000*	Upwind downwind	thin_plate_spline	None
H	Interpolation	1000	Upwind downwind	linear*	None
I	Interpolation	1000	Upwind downwind	cubic*	None
J	Interpolation	1000	Upwind downwind	quintic*	None
K	Interpolation	1000	Upwind downwind	multiquadratic*	None
L	Gradient averaging*	NA	NA	NA	None

TABLE 2.2: Subset of the horizontal advection calculation variations. Case A is the primary method. Cells with asterisks indicate where each case differs from case A.

# Chapter 3

## Results

### 3.1 Estimates of Advective Energy Fluxes

The total advective energy flux across all towers was found to have a mean value of  $-4.42 \text{ W/m}^2$  with a standard deviation of  $146 \text{ W/m}^2$ . The magnitude and signs of the advective fluxes was found to be highly site-dependent with mean values of total advection ranging from  $-78.4 \text{ W/m}^2$  at NW4 to  $30.0 \text{ W/m}^2$  at SW3. The median value of each of the advective flux components, as well as the total advective flux, are given for each tower in Table 3.1. Median advective fluxes are also given as percentages of available energy. It should be noted that since the advective components were divided by available energy at each half-hourly time step before the median was determined, the percentage values are not necessarily representative of the same data point at the raw medians.

Tower	$H_{HA}$	$\lambda E_{HA}$	$H_{VA}$	$\lambda E_{VA}$	Total
WLEF	-0.40 (NA)	1.13 (NA)	(NA)	(NA)	(N/A)
NW1	-0.36 (-0.24)	2.12 (1.60)	31.53 (0.63)	-14.10 (-13.62)	0.93 (-15.96)
NW2	-0.13 (-0.06)	0.04 (0.43)	-4.01 (3.57)	12.30 (12.58)	5.28 (23.51)
NW3	-0.15 (-0.12)	0.12 (0.29)	(N/A)	(N/A)	(N/A)
NW4	-2.15 (-0.07)	2.98 (1.67)	-14.23 (3.13)	-3.43 (5.59)	-14.04 (20.08)
NE1	-1.78 (0.09)	5.38 (0.59)	8.58 (-2.45)	1.57 (-10.85)	13.02 (-18.48)
NE2	1.18 (-0.13)	-0.31 (-0.69)	1.40 (-0.88)	0.03 (0.06)	3.45 (-3.50)
NE3	0.84 (-0.55)	0.94 (-2.55)	-0.63 (0.08)	4.65 (5.85)	13.87 (9.16)
NE4	1.34 (-0.64)	-1.11 (-2.15)	0.54 (0.64)	0.14 (0.05)	-0.90 (-1.17)
SW1	-0.11 (-0.14)	-0.74 (0.22)	-0.54 (0.45)	0.22 (-0.74)	-1.43 (4.36)
SW2	1.01 (-0.32)	-0.34 (-1.08)	-3.49 (3.45)	8.49 (1.8)	-0.11 (15.84)
SW3	0.69 (-0.43)	-1.24 (-0.13)	7.46 (-11.6)	-2.96 (-7.61)	8.24 (-44.60)
SW4	0.35 (-0.28)	-0.68 (-0.87)	0.23 (-10.34)	-30.63 (-5.06)	-20.63 (-40.06)
SE2	-0.05 (0.09)	1.40 (-0.14)	-3.91 (-0.68)	-6.83 (-6.8)	-10.57 (-4.54)
SE3	0.20 (-0.11)	4.16 (-0.48)	-2.53 (2.28)	-0.07 (0.07)	1.89 (5.76)
SE4	-0.06 (0.03)	-0.06 (0.02)	(NA)	(NA)	(NA)
SE5	0.06 (-0.1)	0.05 (-0.09)	0.77 (3.83)	1.63 (4.69)	2.32 (9.15)
SE6	0.37 (-0.17)	0.96 (-0.12)	-1.56 (1.95)	3.57 (10.26)	-0.03 (20.31)

TABLE 3.1: Median values of each component and total advective fluxes for each tower. Values in parentheses are medians of advective fluxes as percentages of available energy.

Vertical advective fluxes of both latent and sensible heat were found to be much larger in magnitude than their corresponding horizontal fluxes. The horizontal advective fluxes found in this study typically constitute less than a couple percent of the available energy. The vertical fluxes vary greatly in value from site to site but are often of substantial magnitude relative to available energy. For 9 of the 15 towers at which vertical advection was calculated, the median value of  $H_{VA}$  and/or  $\lambda E_{VA}$  as a fraction of available energy was greater in magnitude than 5%.

As an example, Figure 3.1 Shows the distribution of values of each of the advective flux components for the NE1 tower. For both  $H$  and  $\lambda E$ , the horizontal advective fluxes are

about an order of magnitude smaller than those of the vertical fluxes. For both vertical and horizontal fluxes,  $H$  and  $\lambda E$  fluxes are of similar magnitude.

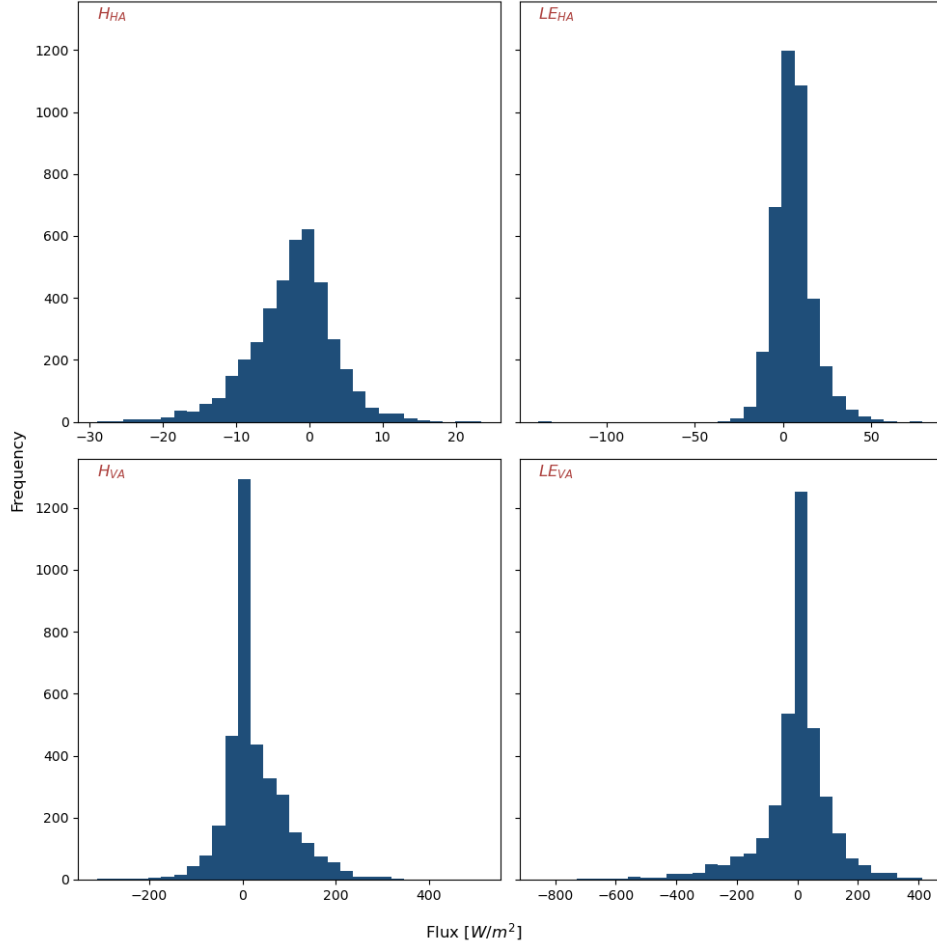


FIGURE 3.1: Histograms showing distribution of half-hourly flux values for each advective flux component. Components shown are, clockwise from top left,  $H_{HA}$ ,  $\lambda E_{HA}$ ,  $\lambda E_{VA}$ , and  $H_{VA}$

## 3.2 Relationships between advective flux components

The difference in magnitudes between the horizontal and vertical advective energy fluxes means that it is not possible for the two to cancel each other out, as has been previously observed with CO<sub>2</sub> fluxes (Aubinet et al., 2003, Yi, 2008). However, in order to investigate

the relationship between horizontal and vertical fluxes, regression lines were fit to  $H_{HA}$  vs.  $H_{VA}$  and  $\lambda E_{HA}$  vs.  $\lambda E_{VA}$ , as shown in Figure 3.2.  $R^2$  values of less than 0.01 were found for both sensible and latent fluxes, indicating that little, if any, relationship exists between horizontal and vertical advection. In spite of the extremely weak correlation, however, the negative slope (-0.57) of the regression line between  $\lambda E_{VA}$  and  $\lambda E_{HA}$  suggests that horizontal and vertical advection of latent heat do tend to be of opposite signs.

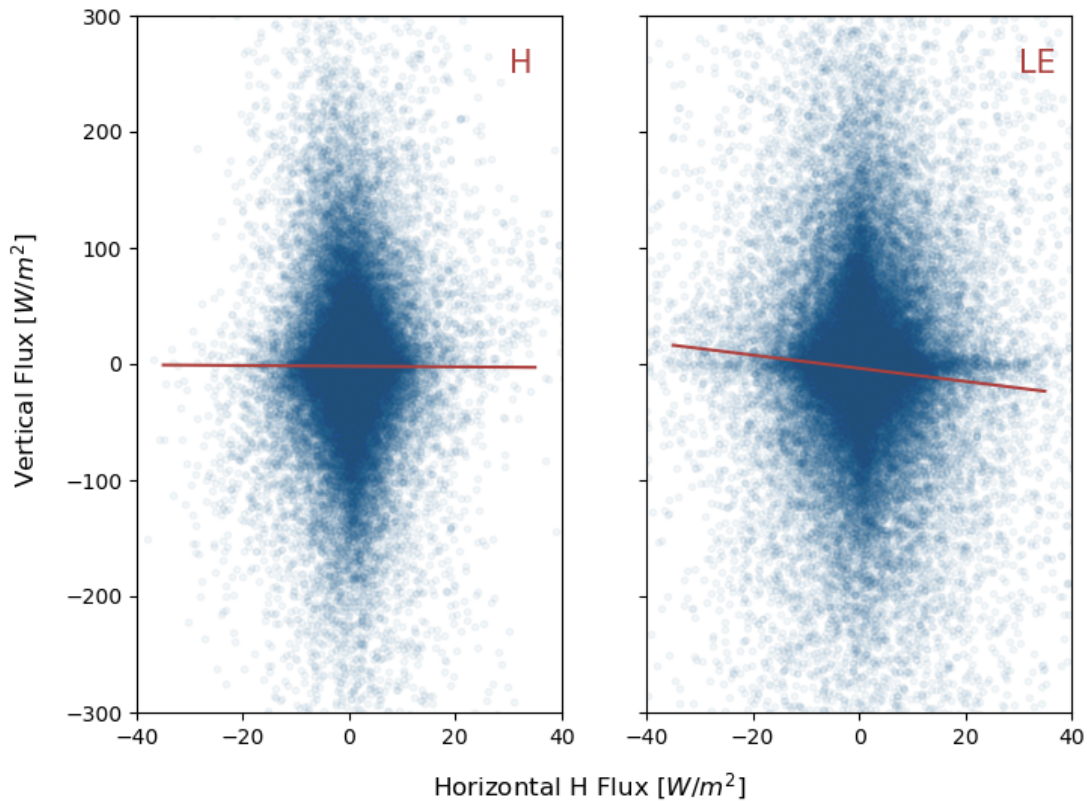
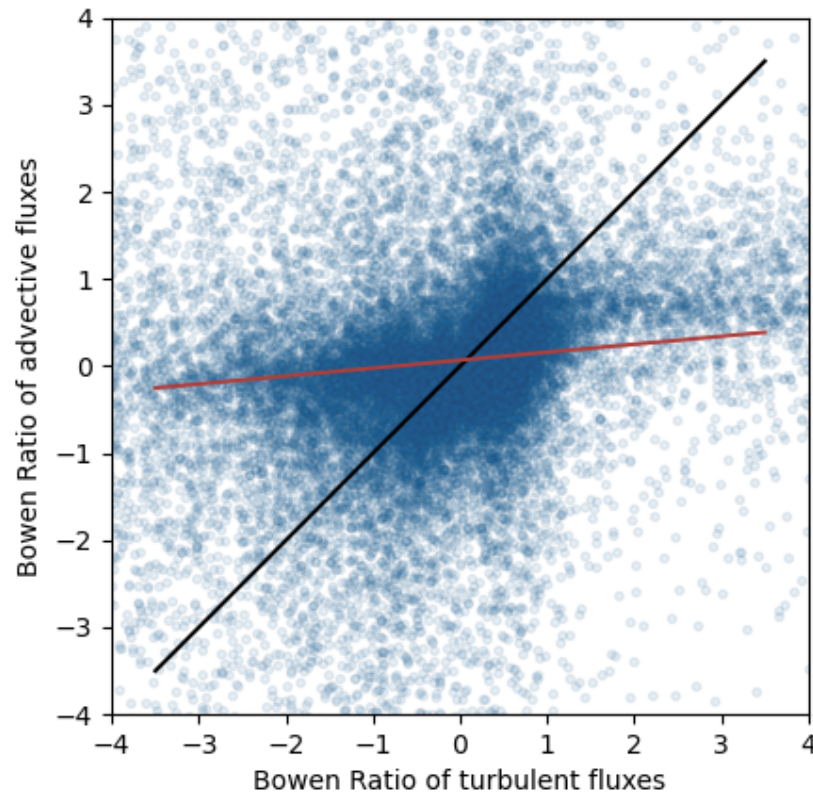


FIGURE 3.2: Scatter plots of horizontal versus vertical advective fluxes of sensible (left) and latent (right) heat. Points are semi-transparent so that the darker areas represent a greater density of points. Best-fit lines are shown in red. Plot ranges have been restricted, cutting off some outliers in order to show the center of the plot in more detail.

A similar investigation of the relationship between the Bowen ratio of the turbulent ( $B_T$ ) and advective ( $B_A$ ) fluxes was carried out. The regression line of  $B_T$  vs.  $B_A$  has a slope of 0.091 and  $R^2$  value of 0.016 (Figure 3.3).



---

FIGURE 3.3: Scatter plot of the Bowen ratios of turbulent vs. advective fluxes. The best fit line is shown in red. The black line has a slope of one, indicating the one-to-one relationship between turbulent and advective Bowen ratios which is assumed by the Bowen ratio closure method.

### 3.3 Effect of Environmental Conditions on Advective Fluxes

At most sites, the latent heat advective fluxes were seen to follow a clear diel cycle (Figure 3.4). Horizontal and vertical advective fluxes of  $\lambda E$  are typically highest in magnitude in the late morning to early afternoon and close to zero at night. The sign of the midday peak, however, is not consistent between towers. For 10 out of 15 sites, the midday peak of  $\lambda E_{HA}$  and  $\lambda E_{VA}$  have opposite signs. For the other 5, they either have the same sign (2 sites), or do not have distinct midday peaks (3 sites). Sensible heat fluxes, both horizontal and vertical, show a less consistent pattern across towers, though many towers show lower sensible heat advection around noon than at other times of day. As a result of these patterns, advection is typically dominated by latent heat around midday and more evenly split between  $H$  and  $\lambda E$  at night.

A seasonal change in advective fluxes over the course of the study was also seen. Figure 3.5 shows the 7-day average total advective flux across all towers. Mean advection tends to increase from around  $-12 \text{ W/m}^2$  in June to near zero in October. The week-to-week variation in mean advection ( $\sigma = 9.8 \text{ W/m}^2$ ) is, however, similar in magnitude to the increase over the course of the study ( $12.8 \text{ W/m}^2$ , based on the slope of the regression line). The 7-day mean of the energy imbalance is also shown in Figure 3.5. The energy imbalance decreases over the course of the study, in line with the decrease in incoming solar radiation from June to October.

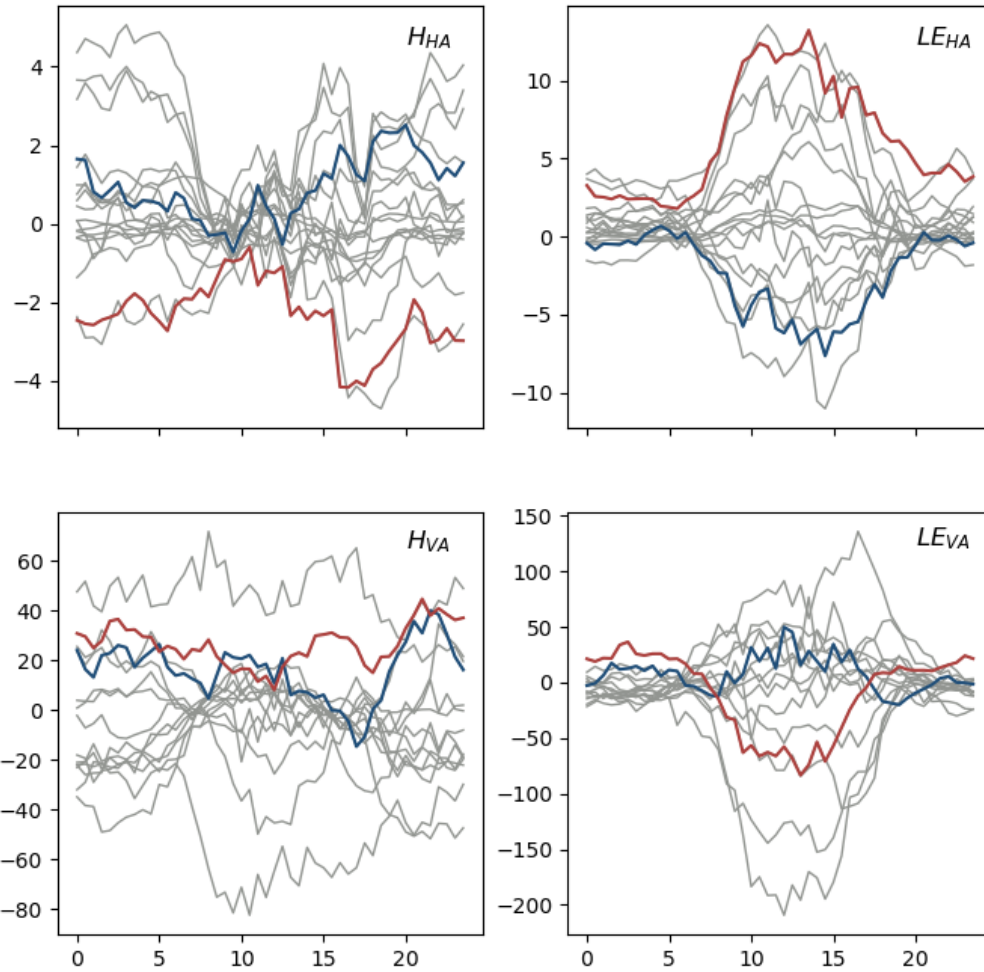


FIGURE 3.4: Average diel cycle of advective fluxes of latent and sensible heat for each tower in gray. Two towers are highlighted in color as examples of the differing sign of the midday peak of  $\lambda E_{HA}$  and  $\lambda E_{VA}$ . Tower NE1 is shown in blue and SW3 in red.

The range of magnitudes of advective fluxes was found to vary with both the atmospheric stability parameter ( $z/L$ ) and friction velocity ( $u_*$ ). Figure 3.6 shows the distribution of total advective flux values, grouped by percentile of  $z/L$  and  $u_*$ . Each grouping contains

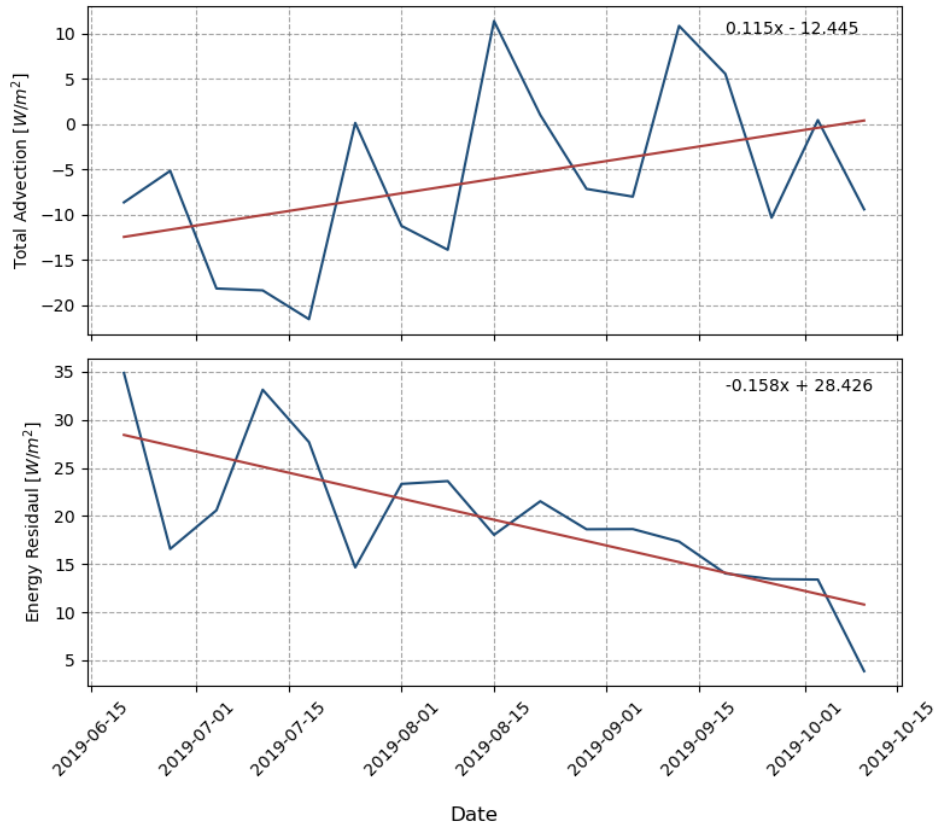


FIGURE 3.5: 7 day averaged total advection and available energy over the course of the CHEESHEAD19 experiment. Regression lines are shown in red with the equation of the line given in the upper right-hand corner. In the regression equations,  $x$  represents the number of days since the start of the experiment, June 20th.

10% of the data points where each bin edge corresponds to the  $(10N)^{th}$  percentile where  $N$  is an integer between 0 and 10. Advective flux values tend to be smaller in magnitude when the atmosphere is weakly stable or near neutral. The range of observed advective fluxes increases under increasingly stable or unstable conditions. However, under extremely unstable conditions ( $z/L < -0.819$ ), the range of magnitudes of advective fluxes is lower than for low to moderate instability ( $-0.819 \leq z/L < -0.0287$ ). In relation to the friction velocity, the lowest range of advective flux values is observed for moderate  $u_*$  values ( $0.189 \leq u_* < 0.396$ ). Magnitudes of advective fluxes increase as  $u_*$  becomes

more extreme in either direction. The greatest range of advective fluxes was observed in the highest  $u_*$  group ( $0.741 \leq u_* < 1.593$ ). Under low  $u_*$  conditions, there is shift towards more negative advective fluxes. The median total advective flux value for the lowest  $u_*$  group ( $0 \leq u_* < 0.0689$ ) was  $-11.5 \text{ W/m}^2$ , as opposed to  $2.30 \text{ W/m}^2$  for the 40<sup>th</sup> - 50<sup>th</sup> percentile group ( $0.253 \leq u_* < 0.320$ ).

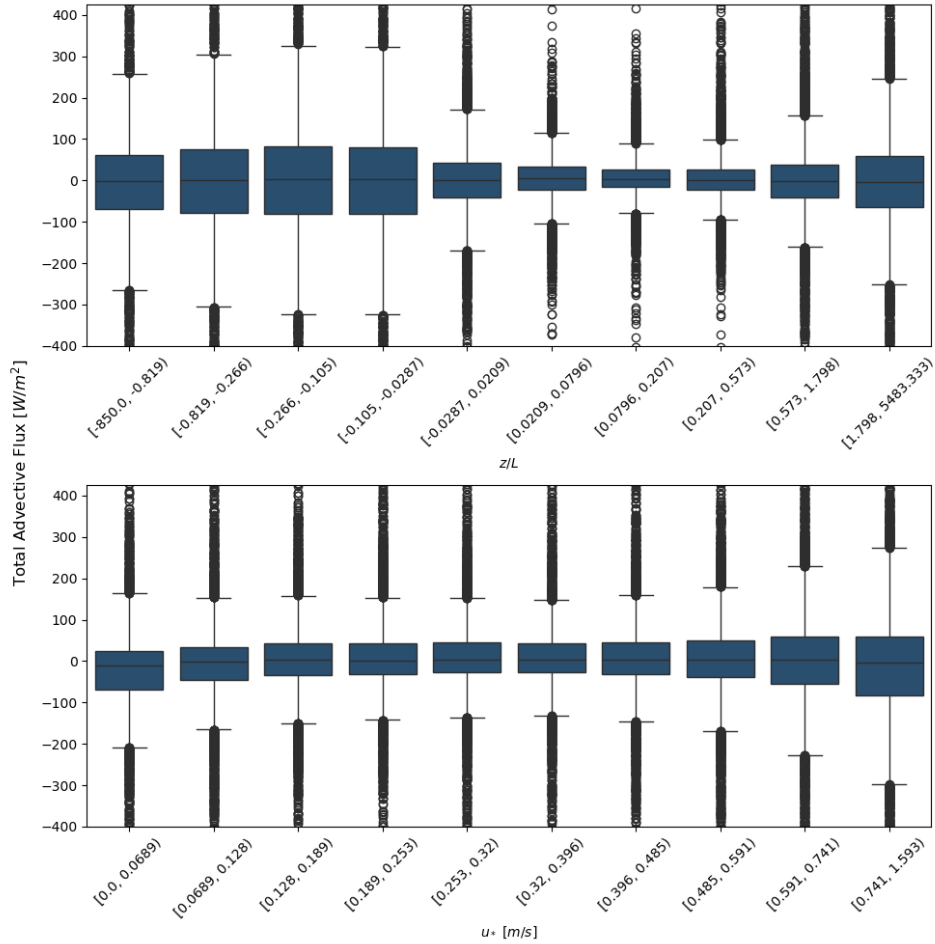


FIGURE 3.6: Top: Box plot showing relationship between stability parameter ( $z/L$ ) and total advective flux. Advective fluxes were grouped by  $z/L$  value.  $z/L$  bins edges were set according to the percentiles such that 10% of measurements fall into each bin. Bottom: same as top but with friction velocity ( $u_*$ ) in place of  $z/L$ .

### 3.4 Contribution of Advective Fluxes to Energy Budget Closure

Figure 3.7 shows the average values of  $Imb_{NA}$  and  $Imb_A$  for each tower. The average energy imbalance decreased for 10 of the 15 towers when all components of the advective fluxes were calculated. Of these, six showed improved energy budget closure, in that the mean absolute value of  $Imb_A$  was less than that of  $Imb_{NA}$  ( $EBI > 0$ ). For the remaining four, the advective energy fluxes over-corrected for the energy imbalance resulting in negative mean  $Imb_A$  values of similar or greater magnitude to  $Imb_{NA}$ . For five of the towers, the mean energy imbalance increased. These corresponded to  $EBI$  values ranging from -18% at SE3 to -477% at SW4 when using the time-averaged imbalance values to calculate  $EBI$ .

Across all towers, the energy imbalance decreased for 28.6% of site-hours when all advective energy fluxes were included. 25.5% of site-hours had an  $EBI$  greater than 10%. Figure 3.8 shows the percent of site-hours where the energy balance was improved, relatively unchanged, or made worse, grouped by hour of the day. The percent of site-hours with positive  $EBI$  was lowest during nighttime hours and highest in the morning. An  $EBI > 10\%$  was observed during 35.7% of site-hours at 08:00 as compared to only 9.5% of site-hours at 01:00. Additionally, a larger percent of site-hours fell under the category of “relatively no change” ( $-10\% < EBI < 10\%$ ) during the daytime than at night. This indicates that the total advective flux is typically larger relative to the energy imbalance

at night than during the day.

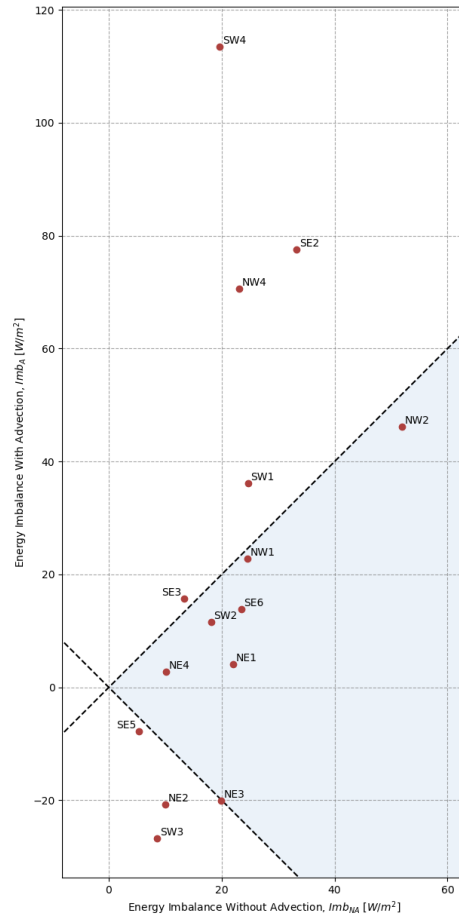


FIGURE 3.7: Scatter plot of mean  $Imb_{NA}$  vs.  $Imb_A$  for each tower. Blue region bounded by dashed lines represents an improvement in energy balance closure as defined by the absolute value of  $Imb_A$  being lower than  $Imb_{NA}$

### 3.5 Case Evaluation

Of the two periods outlined in section 2.5, the total advective flux at NE1 was found to have a moderate positive correlation with  $Imb_{NA}$  during P1 (slope = 0.803,  $R^2 = 0.602$ ).

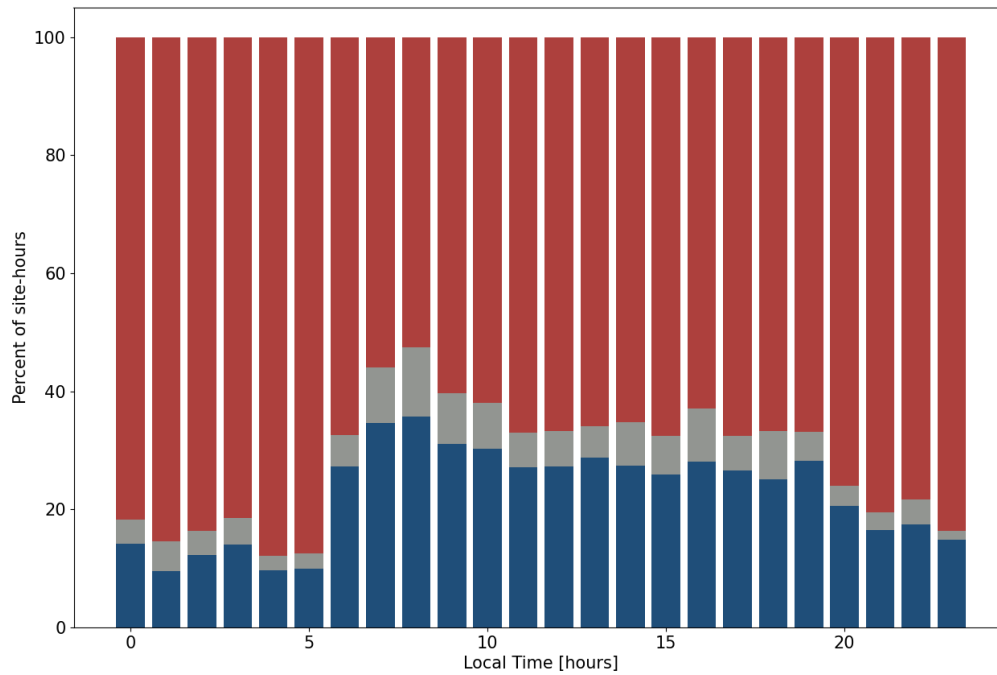


FIGURE 3.8: Percent of site-hours when energy balance was improved (blue), relatively unchanged (gray), or made worse (red) by the inclusion of advective energy fluxes. Unchanged site-hours defined as a change of less than 10% of  $Imb_{NA}$ .

During P2, the correlation was slightly weaker and negative (slope = -2.02,  $R^2 = 0.516$ ). Figure 3.9 shows the relationship between advective flux total and energy imbalance for both P1 and P2 at NE1.

P1 was identified for the strong correlation between total advection and  $Imb_{NA}$  at tower NE1 without consideration of other towers. In order to investigate whether the improved energy balance during this period was due to domain-scale conditions, the average energy imbalance, with and without advective fluxes, was found for other towers during this period. Figure 3.10 shows the average values of  $Imb_{NA}$  and  $Imb_A$ , both for the entire

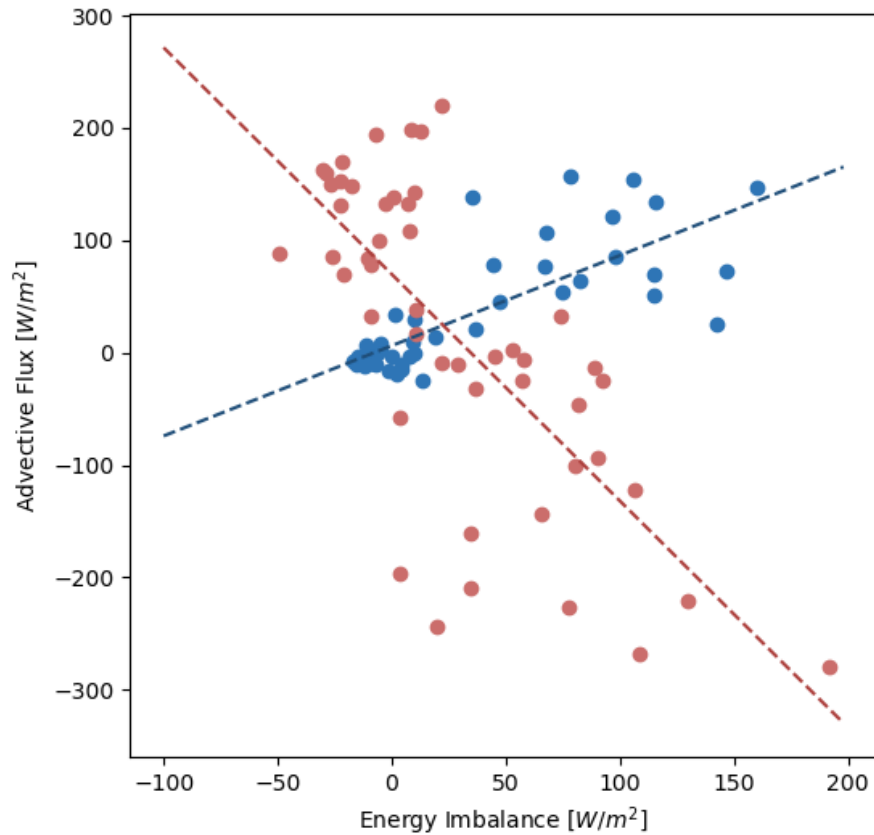


FIGURE 3.9: Scatter plot of Imb vs. total advective flux for P1 (blue) and P2 (red). Best fit lines for each period are shown as dashed lines in the same color as the scatter plot points.

study period and for P1 for six towers including NE1. Only towers missing less than 25% data (12 out of 48 timesteps) during P1 are shown in Figure 3.10. While the energy imbalance is essentially eliminated for NE1 ( $Imb_A = 0.84\text{W/m}^2$ ), this is not true at other sites. In fact, for NE4 and SW2, energy balance improves due to the advective fluxes over the entire study period but worsen during P1.

Given the high level of agreement between the total advective fluxes and energy imbalance

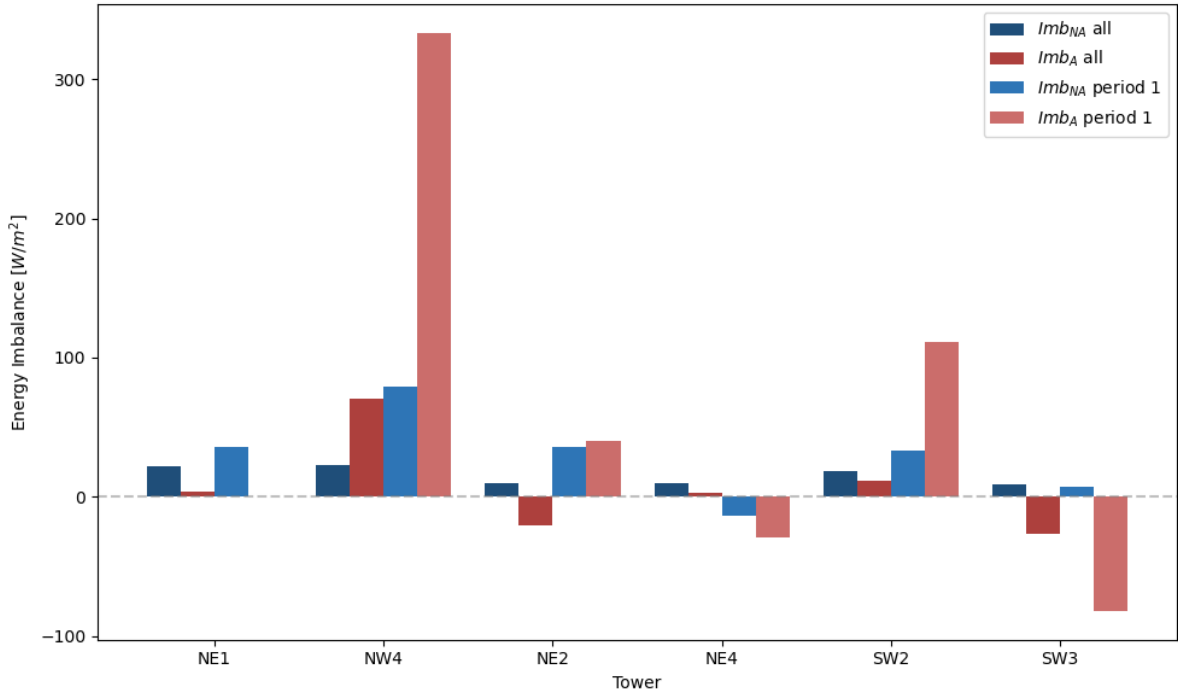


FIGURE 3.10:  $Imb_{NA}$  and  $Imb_A$  for P1 and the entire extent of CHEESEHEAD study.  $Imb$  values are shown for 7 towers which had data for at least 75% of timesteps during P1: NE1, NW4, NE2, NE4, SW2, and SW3

at site NE1 during P1 (NE1P1), we suspect that the calculated NE1P1 advective fluxes may be more representative of the true advective fluxes than at other times and sites. This provides the opportunity to re-investigate the relationships tested in section 3.2 while potentially eliminating some of the noise due to errors in the advective flux calculations. Figure 3.11 and Figure 3.12 are the same as Figure 3.2 and Figure 3.3, respectively, except that only data from NE1P1 is shown, rather than all sites over the entire study period. Here, somewhat stronger relationships between advective flux components were seen (Figure 3.11). For NE1P1,  $H_{HA}$  and  $H_{VA}$  were found to be negatively correlated with an  $R^2$  value of 0.177.  $\lambda E_{HA}$  and  $\lambda E_{VA}$ , however, had a weaker correlation ( $R^2 = 2.8 \times 10^{-3}$ ) for NE1P1 than across the entire study. The best-fit line between  $B_T$  and  $B_A$

for NE1P1 was found to have a slope of 0.356 and  $R^2$  of 0.388 (Figure 3.12). While the slope for NE1P1 is greater than that found across all towers and days, both slopes are significantly less than 1.

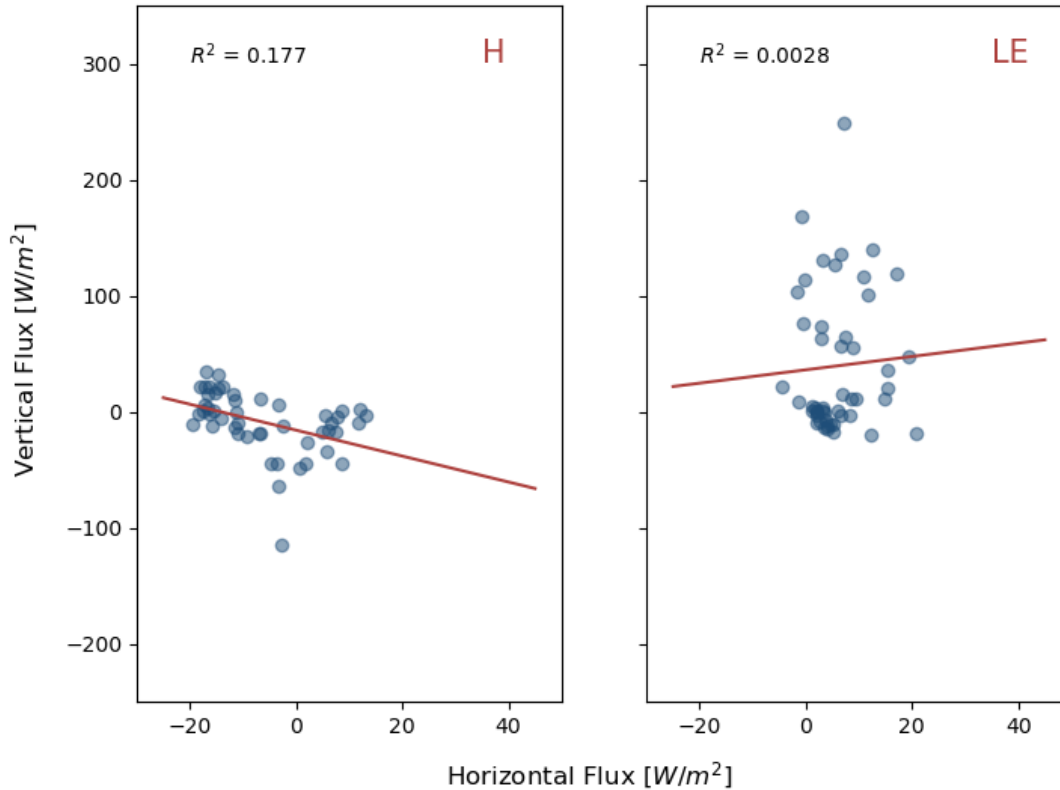


FIGURE 3.11: Same as Figure 3.2, except only for NE1P1.

### 3.6 Sensitivity to calculation method

For each of the cases defined in table 2.2, the total horizontal advective flux ( $H_{HA} + \lambda E_{HA}$ ) was plotted against the total horizontal advective flux from Case A (Figure 3.13). In the bottom right panel, vertical advection calculated using  $\bar{w}$  from the continuity equation is

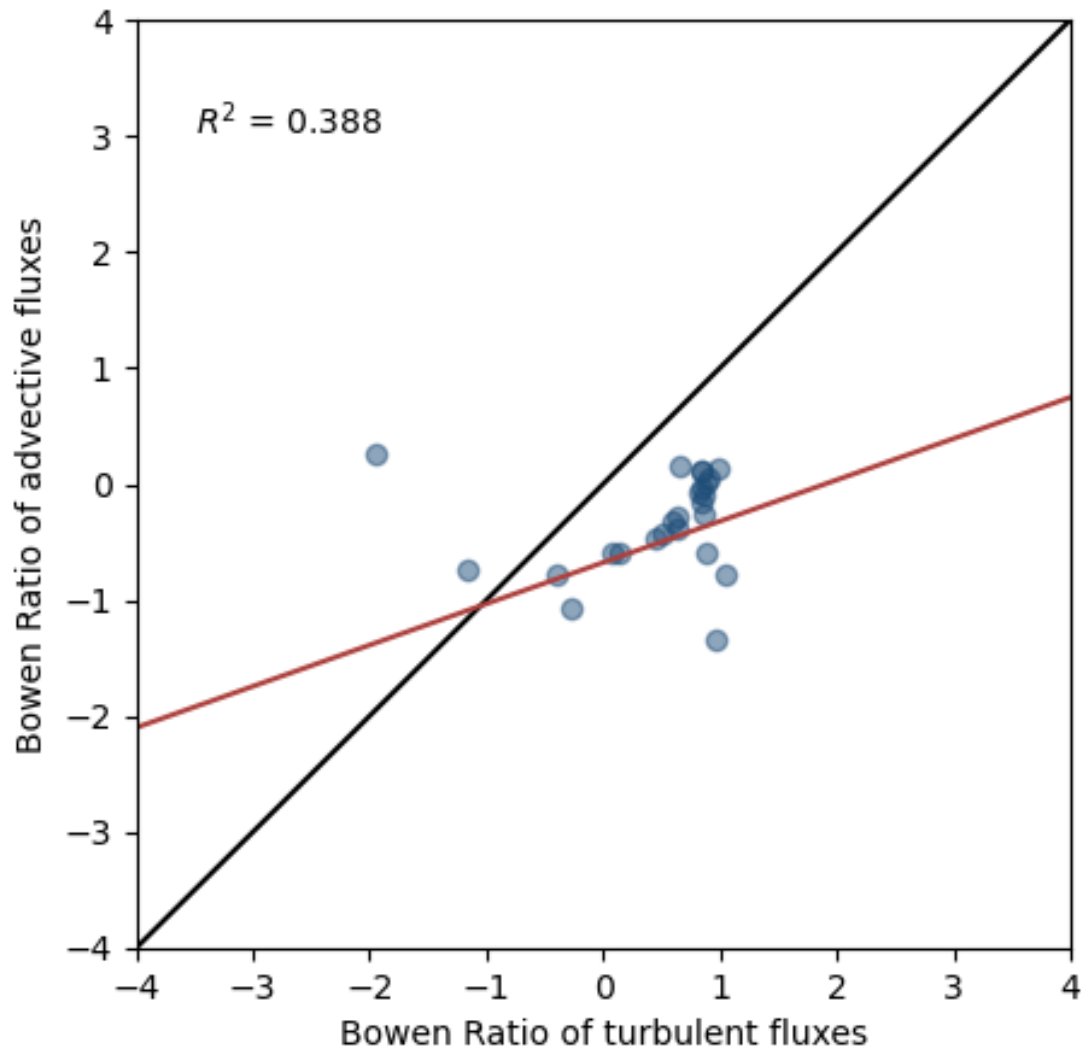


FIGURE 3.12: Same as Figure 3.3, except only for NE1P1.

plotted against vertical advection from the sonic anemometer. For each pair of cases, the root mean square difference (*RMSD*) was calculated.

For Case B, which differs from Case A by the inclusion of the stability parameter defined in Benoit (1977), the horizontal fluxes agree well with Case A for most data points. There

is, however, a set of points for which the Case B fluxes are near zero regardless of the value from Case A.

Of all the cases in Table 2.2, Case C agrees most closely with Case A ( $RMSD = 0.7W/m^2$ ) indicating that the direction from the tower in which the interpolation points are located has little impact on the calculated horizontal advection.

Cases D through G differ in the distance of the interpolation points from the towers. Agreement with case A decreases as the interpolation distance is made smaller or larger than the Case A distance of 1 km. Shorter interpolation distances generally result in larger horizontal advective fluxes while greater distances lead to smaller advective fluxes.

Different interpolation kernel function types were used in cases H through K. Of the kernels tested, linear, cubic, and multiquadratic (Cases H, I, and K respectively) resulted in a similar level of agreement with the Case A thin plate spline function ( $RMSD$  between  $4.77 W/m^2$  and  $4.92 W/m^2$ ). Cases H and K produced horizontal advective fluxes that were smaller in magnitude than Case A while Case I produced larger magnitude fluxes. The magnitudes of fluxes calculated by Case J (quintic kernel) were often much larger in magnitude, sometimes by an order of magnitude or more, than Case A. The  $RMSD$  for case J was  $47.08 W/m^2$ .

Aside from Case J, Case L, which used the gradient averaging method, was the least consistent with Case A horizontal advective fluxes ( $RMSD = 8.26 W/m^2$ ).

For the vertical advective fluxes, use of  $\bar{w}$  from continuity produced very different advection estimates than  $\bar{w}$  from the sonic anemometer. The *RMSD* value of 272.5 W/m<sup>2</sup> is greater than the standard deviation of either estimate of the total vertical advective fluxes (149.9 W/m<sup>2</sup> and 203.4 W/m<sup>2</sup> for the sonic and continuity methods, respectively).

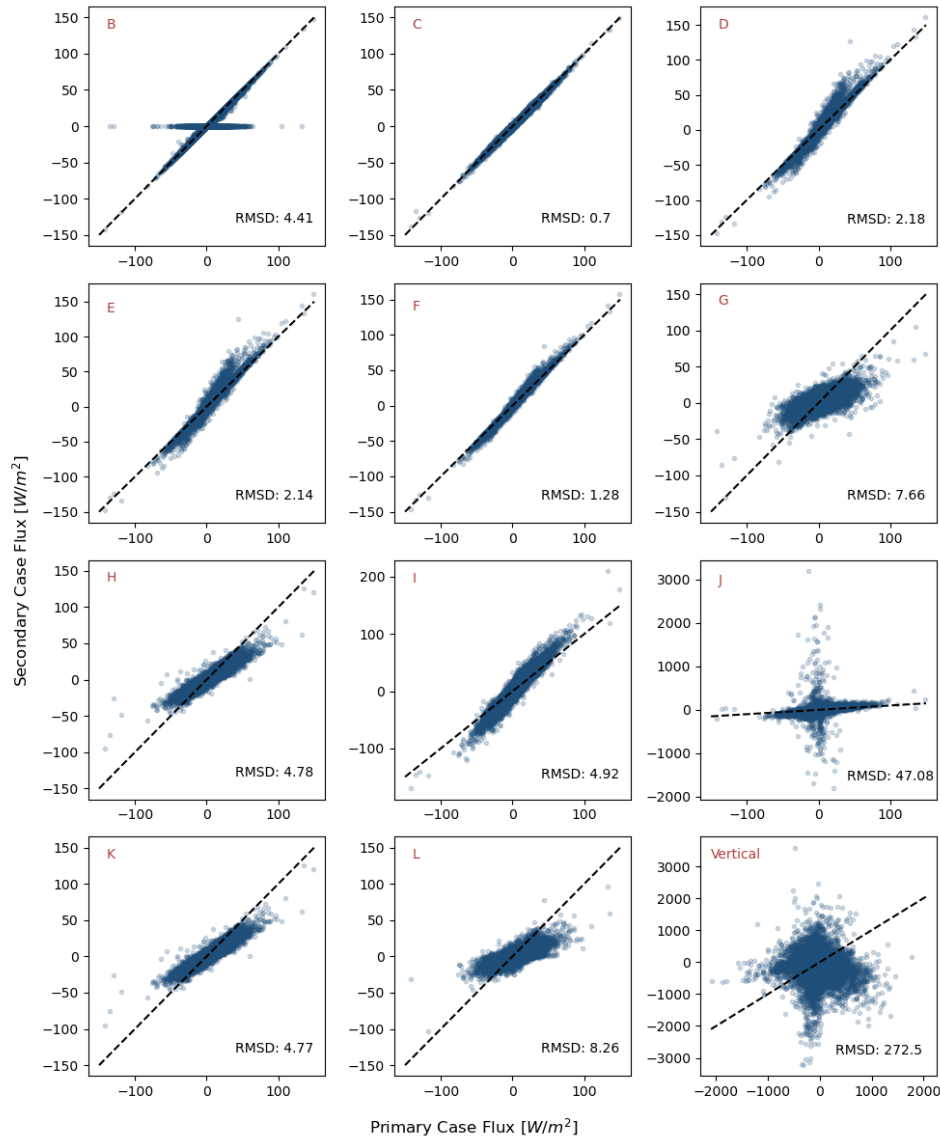


FIGURE 3.13: Scatter plots of horizontal advective fluxes for each half-hour measurement period for case A v. each case variation listed in Table 2.2. Bottom right panel shows vertical advection using sonic anemometer-derived  $\bar{w}$  v. vertical advection from continuity. Regression lines are shown in black on all plots.

When horizontal and vertical advection are combined, the differences in vertical advection estimates dominate the overall pattern of advective fluxes. Figure 3.14 shows the mean diel cycle of all 204 calculation variations. The two vertical advection calculation methods separate the cases into two distinct groups with nearly no overlap. While the advective fluxes calculated using the continuity approach tend to be lower than those using the sonic measurements, the two groups follow a similar pattern during the day. At night, however, the two estimates diverge to the extent that the signal of the diel cycle is overwhelmed by differences between estimates. Within the two groups, the greatest spread between different cases is observed around midday followed by late evening hours. The best agreement between cases is seen in the mid morning and late afternoon.

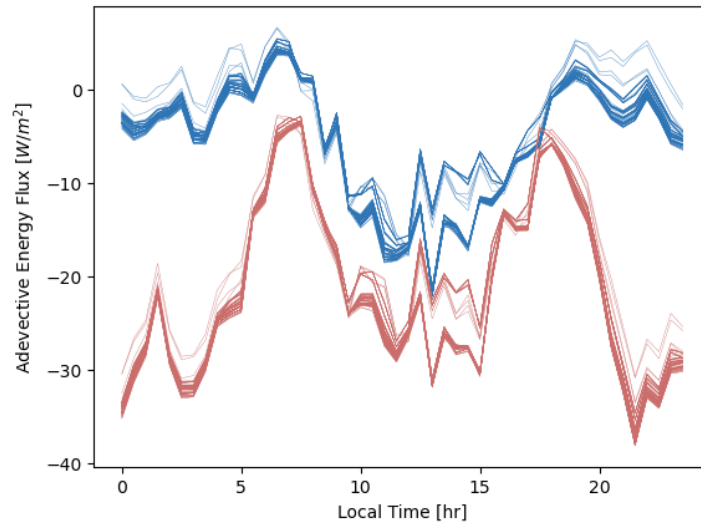


FIGURE 3.14: Average diel cycle of total advective energy flux for each of the 204 calculation variations (as outlined in Figure 2.5). Advection estimates using sonic-derived  $\bar{w}$  are shown in blue while estimates from continuity-derived  $\bar{w}$  are shown in red.

# Chapter 4

## Discussion

While a number of studies have attempted to quantify advective energy fluxes, doing so is a notoriously challenging task. The lack of spatially-dispersed measurements prevents the estimation of advective fluxes at most EC flux sites. In addition, advective flux estimates often contain a high degree of scatter making it challenging to identify relationships. As a result, there are still many open questions with regards to how advective motions transport energy between the surface and atmosphere and how to best quantify this transport. In this study, we attempt to further the understanding of the nature of advection by estimating advective energy fluxes from measurements taken during the CHEESEHEAD19 field campaign. We examine the relationships between individual advective flux components as well as the impact of environmental conditions and calculation methodology on advective fluxes. We further investigate the contribution of advective energy fluxes to the overall surface energy balance closure.

Many other advection studies have focused on limited cases where advective transport is enhanced or more predictable such as in sloped terrain or at homogeneous sites downwind of a land surface transition. In contrast, the CHEESEHEAD19 dataset offers the opportunity to study advection in a highly heterogeneous landscape with variation in vegetation type, roughness length, topography, and surface heating, on a variety of scales across the domain. Further, the horizontal scale of the CHEESEHEAD19 domain exceeds that of other advection studies that have used in situ measurements to estimate horizontal advective fluxes. This may allow for the quantification of advective transport due to larger scale motions or heterogeneity that may be missed by studies using measurements with a more limited horizontal range.

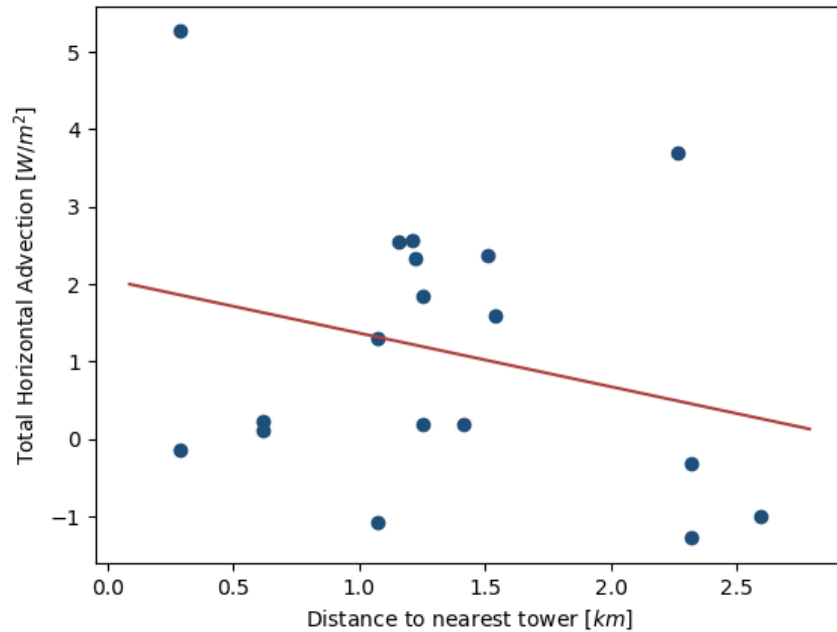
## 4.1 Estimates of advective fluxes

The difference in magnitudes of the horizontal and vertical advective fluxes found in this study suggests vertical advection plays a much more substantial role in the surface energy balance than horizontal advection. This finding might support the neglect of horizontal advection at similar sites where surface heterogeneity is somewhat isotropic, as opposed to the site being located adjacent to a singular surface change, or on a steep slope leading to persistent up or down slope winds. However, this difference in magnitudes may instead be indicative of a systematic error within our estimates. Other studies such as Moderow et al. (2021) have found more comparable magnitudes between horizontal and vertical advection.

The vertical advective fluxes found here are somewhat larger than those found in other studies (Moderow et al., 2021, Morrison et al., 2021) which may indicate that they were overestimated. In addition, vertical advective fluxes greater in value than the available energy were found on numerous occasions. True advective fluxes of this magnitude are unlikely suggesting, again, that the vertical fluxes may be overestimated. Lee (1998) notes the challenge of accurately estimating  $\bar{w}$  from sonic anemometer measurements. Due to the near-zero typical  $\bar{w}$  values, a small absolute error can lead to large relative errors in  $\bar{w}$  and vertical advection. Others have observed a high degree of scatter and unrealistic vertical advection value when using sonic  $\bar{w}$  measurements (Feigenwinter et al., 2008, Wang et al., 2024). It may be that the use of the sonic anemometer measurements led to an overestimation of vertical advective fluxes in this study. On the other hand,  $H_{VA}$  and  $\lambda E_{VA}$  were found to be typically even larger in magnitude when  $\bar{w}$  was estimated using continuity rather than the sonic measurements.

It is also possible that the horizontal advective fluxes found in this study were underestimated. As noted by Cuxart et al. (2016) and Garcia-Santos et al. (2019), gradients in surface temperature due to heterogeneities on the hectometer scale are the most important contributors to horizontal sensible heat advection. The horizontal spacing of towers in the CHEESEHEAD study was most appropriate to capture surface heterogeneities on the kilometer scale. It may be that a greater density of measurements would be needed in order to capture the appropriate scale of horizontal heterogeneity and advective fluxes. This idea is supported by our finding that the magnitude of horizontal advective flux estimates increases with decreased interpolation distance, indicating that there are larger

horizontal gradients on smaller spatial scales. Our ability to capture this effect, however, is likely limited by the density of the towers within the CHEESEHEAD domain. Figure 4.1 shows the relationship between mean total horizontal advection at each tower site and the distance to the nearest tower. The relationship is weak ( $R^2 = 0.070$ ), but negative indicating that proximity to other towers, and thus increased resolution of horizontal heterogeneity, leads to greater horizontal flux estimates.




---

FIGURE 4.1: Scatter plot of distance from each tower to the nearest tower vs. total horizontal advective energy flux ( $H_{HA} + \lambda E_{HA}$ ). Regression line shown in red.

## 4.2 Relationships between advective flux components

Past studies have found that horizontal and vertical advection of CO<sub>2</sub> often offset each other, particularly under stable night time conditions at sloped sites (Aubinet et al.,

2003, Yi, 2008). Our findings suggest that this relationship is not universally applicable to advective transport of other tracers and under different conditions. Interestingly, over the entire study, the  $\lambda E_{HA}$  and  $\lambda E_{VA}$  were more strongly correlated than  $H_{HA}$  and  $H_{VA}$  while the reverse was found to be true for the period NE1P1. This may indicate that any correlation between horizontal and vertical advective fluxes is highly dependent on site or conditions.

A weak positive correlation was found between  $B_T$  and  $B_A$ . Any conclusions drawn from this relationship must be taken cautiously given the previously discussed indications of potential error in the advection estimates. However, The lack of correlation and non unity slope of the regression line between  $B_T$  and  $B_A$  both suggest that using  $B_T$  to partition the energy residual is an appropriate method to close the surface energy balance. For both the entire study and the NE1P1 subset, the best fit line between  $B_T$  and  $B_A$  has a slope well below 1, indicating that the Bowen ratio of the advective fluxes is typically lower in magnitude than that of the turbulent fluxes. This is contrary to the findings of Paleri et al. (PREPRINT) who found, using a large eddy simulation based on the CHEESEHEAD19 field campaign data, that SCs contribute more to the transport of sensible than latent heat. On the other hand, our results are consistent with the findings of Eder et al. (2014) who found that the Bowen ratio closure method typically underestimates latent heat flux. In contrast to their results, however, we did not find  $B_T$  to be a reasonable estimate of  $B_A$  when  $B_T$  is close to 1.

### 4.3 Effect of environmental conditions on advective energy fluxes

In investigating the diel cycle of the advective flux components (Figure 3.4), latent heat fluxes were found to have a more distinct diel cycle than sensible heat fluxes. Daytime fluxes of  $\lambda E$  were found to be much larger in magnitude than those observed at night. This aligns with the typical diel cycle of turbulent latent heat flux. Unlike the turbulent flux, however, for about half of the towers in the CHEESEHEAD domain, the midday peak of  $\lambda E$  advective fluxes is negative in sign. The gradients which drive  $\lambda E$  advection are strongest around midday when evapotranspiration, peaks. The lack of consistency between the signs of  $\lambda E_{HA}$  and  $\lambda E_{VA}$  across sites implies that the advective fluxes are driven by gradients and motions on scales significantly smaller than the CHEESEHEAD domain. This is further evidence that the scale of heterogeneity most relevant to the advective fluxes may not be sufficiently resolved by the 18 towers used in this study.

Over the course of the study, advective fluxes increase from a negative weekly mean value in June to near zero in October. Over the same period, the positive energy residual decreases, though it is not completely eliminated. Both of these patterns suggest a decrease in transport by way of SCs. However, the negative mean advective flux observed at the beginning of the study serves to increase the energy imbalance on average. This indicates the methods used in this study to estimate advective fluxes may, on average, capture the magnitude transport by SC with some realism. It appears, however, that the

sign of the estimated advective fluxes is often incorrect. There is a strong week-to-week variation in the mean total advection, as shown in Figure 3.5. This may be explained by some yet unidentified driver of advective fluxes. On the other hand, given the other evidence of a large degree of uncertainty in the advection estimates, this variation around the trend may simply be attributed to error in the estimated fluxes rather than variation in the true fluxes.

Some previous studies have found that the energy imbalance is smallest under near neutral or weakly stable conditions and increases under increasingly unstable conditions (Butterworth et al., 2024, Lindroth et al., 2010, Stoy et al., 2013, Zhou and Li, 2019) while others have reported a decrease in energy imbalance under highly unstable conditions (Mauder et al., 2010, McGloin et al., 2018). The calculated advective fluxes in this study seem to follow a pattern that is a hybrid of these observations, with the largest advective fluxes occurring under moderately unstable conditions. However, substantial advective fluxes were also found under strongly stable conditions in this study, a pattern that has not been reported for absolute energy imbalance in other studies. This may suggest that under unstable conditions, advective fluxes are an important component of the energy imbalance while the relationship between the two is less clear under stable conditions. This is consistent with the understanding that secondary circulations, which form most readily under unstable conditions, are the primary driver of advective fluxes.

The relationship between advective fluxes and  $u_*$  found in our study is consistent with

patterns of energy imbalance in other studies under low  $u_*$  but diverges from these patterns under high  $u_*$  values. Greater advective fluxes were found under low  $u_*$  conditions, in line with the increase in  $Imb$  typically found with decreasing  $u_*$  (Barr et al., 2006). However,  $Imb$  has not been noted to increase under high  $u_*$  conditions, as was observed with the advective fluxes in this study. This is indicative of a divergence between advective fluxes and energy imbalance under these conditions. This could be due to greater error in the advective flux estimates under these conditions, or to the larger advective fluxes being offset by some other energy budget component, resulting in a lower energy residual.

#### 4.4 Contribution of advective fluxes to energy budget closure

The calculated advective fluxes did not consistently improve energy balance closure. This implies either a substantial degree of error in the advection estimates, or that advective energy fluxes are not the primary reason for energy balance non-closure. Given the large body of evidence suggesting that transport by way of SCs is responsible for at least some portion of the surface energy imbalance, particularly under heterogeneous surface conditions, the former is the more likely explanation for our observations.

Improved energy balance closure was achieved at 6 of 15 sites when considering  $Imb_{NA}$  and  $Imb_A$  averaged over the entire study period. However, at no site was the energy imbalance improved during more than 50% of half-hour measurement periods. Energy balance was

shown to improve more often during the day, and especially in the morning, but this peaks with 35.7% of site-hours improved at 08:00. These results suggest that while the method used here may work better under certain conditions than others, substantial error in the estimates is ubiquitous.

## 4.5 Sensitivity to calculation method

The analysis of the sensitivity of the calculated advective fluxes to variations in methodological choices revealed that certain methodological choices can have a substantial impact on the results. While a spread of possible advection estimates was found here, further investigation is needed to identify which method produces the most accurate advective flux estimates.

Of the variations to the horizontal interpolation method, the choice of interpolation kernel was found to have the most significant effect on the calculated fluxes. Certain kernels lead to systematically larger advection estimates indicating that the choice of kernel could potentially lead to a systematic over or underestimation of the fluxes. The true value of the advective fluxes is unknown, preventing the identification of the most accurate estimate. The quintic interpolation kernel produced advection estimates which agreed poorly with the other function types and were, at times, unrealistically large in magnitude suggesting that it is an unsuitable kernel choice for this application. A better understanding of which function type best captures the true spatial variation in temperature and humidity across the domain is needed. This could be tested by removing some data points from

the interpolation input, estimating measurement values at those towers, and comparing to the measured values.

The difference between cases with different interpolation distances, as discussed above, indicate that gradients on scales smaller than a kilometer may lead to larger horizontal gradients, and thus larger flux estimates, than those on the kilometer scale. This suggests that the spatial density of the data used in this study may not be sufficient to fully capture the magnitude of the horizontal advective fluxes.

A moderate difference was found between horizontal energy advection calculated using gradients derived from the interpolation and the gradient averaging methods. This method has the advantage that it does not allow for variations such as those discussed above for interpolation. This may serve to eliminate the opportunity for compounded errors caused by multiple improper methodological choices. On the other hand, the assumption to decompose gradients between the  $x$  and  $y$  directions based solely on offsets in either direction is likely not accurate in most cases. The error that results from this assumption may be averaged out for towers near the middle of the domain with a relatively even distribution of towers in all directions but is more likely to cause bias at towers near the edge of the domain. The horizontal flux values found using this method tend to be smaller than those calculated by the primary interpolation method. This suggests that this method for decomposing the gradients may not allocate a large enough portion of the gradient to the wind-parallel direction.

The estimate of vertical wind speed had by far the most substantial effect on the total calculated advective fluxes. Most vertical advection studies use sonic anemometer measurements of  $\bar{w}$  due to the lack of other measurements. Here, the horizontal wind measurements taken across the 18 towers used in this study allowed us to compute a second estimate of vertical wind, and thus vertical advection. Energy balance closure being the only gauge available for assessing the performance of different methods, results suggests that the sonic-derived fluxes better estimate the true vertical advection than those from continuity.

While substantial differences exist between the various case estimates, the impact of methodological variations on overall energy balance closure is less pronounced. Regardless of methodology, the advective fluxes worsen energy balance closure more often than they improve it. This suggests that the measurements used here may not be sufficient to accurately estimate advective fluxes. This may be due to a combined effect of measurement error and the lack of spatial resolution of the measurements. However, methodological choices made in calculating the advective fluxes does have a substantial impact on the advective flux estimates. Further investigation is needed to identify which of the presented methods, or others untested in this study, best approximates the true advective fluxes.

## Chapter 5

### Conclusion

In this study, we estimated advective energy fluxes using measurements taken at 18 flux towers during the CHEESEHEAD19 study. These advective fluxes were found to typically be reasonable in value. However, there is some evidence that horizontal fluxes may be underestimated while vertical fluxes may be overestimated. In particular, as has been found in other studies, the vertical advective fluxes calculated from the vertical wind measured by the sonic anemometer are, at times, unreasonably large.

Horizontal and vertical advective fluxes were not found to offset each other, contrary to findings in some other studies. Further, the Bowen ratio of the turbulent fluxes was found to be a poor estimate of the Bowen ratio of the advective fluxes. Using the turbulent Bowen ratio to force energy balance closure was found to lead to underestimates of advective  $\lambda E$  fluxes and overestimates of advective  $H$  fluxes.

The advective  $\lambda E$  fluxes here follow a more clear diel cycle than  $H$ . Further, in this study,  $\lambda E$  advection dominates the total advective flux during the day, while  $\lambda E$  and  $H$  have similar contributions at night. Advective fluxes were found to decrease in magnitude over the course of the study, from June to October, in line with the decreasing energy imbalance. The relationship of advective fluxes with atmospheric stability and friction velocity generally aligned with energy imbalance patterns found in other studies. One significant exception to this was that the advective fluxes increased as  $u_*$  increased from moderate to high values while energy imbalance has been observed to decrease with increasing  $u_*$ .

The calculated advective fluxes did not, overall, improve energy balance. While energy balance closure was improved for about a quarter of site-hours, the advective fluxes more often served to increase energy imbalance. This indicates that the measurements collected at the CHEESEHEAD19 tower sites may not be sufficient to accurately estimate advective fluxes under all conditions. Improvement in energy balance closure was, however, shown to be greatest during the daytime, especially in the morning. This could be related to the different scales of atmospheric motions that typically occur at different times throughout the diel cycle. Further investigation of the conditions under which the calculated advective fluxes increase or decrease energy balance closure may lead to an improved understanding of the nature of advective fluxes and their contribution to the surface energy balance.

The sensitivity of the calculated advective fluxes to a number of methodological choices was assessed. Of these, the method used to determine mean vertical wind velocity was

found to have the most substantial impact on total advective flux estimates.  $\bar{w}$  measured using the sonic anemometer appears to produce more realistic results than  $\bar{w}$  calculated from the continuity equation. While significant scatter is observed in both vertical advective flux estimates, fluxes calculated using sonic  $\bar{w}$  measurements more often improve the energy balance closure. The variations in horizontal advection calculations have a moderate impact on total advection estimates for individual half-hour measurement periods. They have little impact, however, on the overall energy balance closure. This indicates that improved  $\bar{w}$  measurements may be the most important advancement needed to increase the accuracy of advective flux estimates, and thus improve energy balance closure.

Overall, our results indicate that a dense tower network may be used to detect advective fluxes and provide insight into the behavior of advective transport. Additional observations including a greater spatial density of  $T$  and  $q$  measurements and an alternative estimate of  $\bar{w}$ , such as from wind LiDAR, may be beneficial in improving advective flux estimates. In addition, the substantial energy imbalance at most sites after the inclusion of advective energy fluxes suggests that accurate estimation of advective fluxes may not be sufficient to close the energy budget. Further work is needed to better understand when energy balance non-closure is primarily due to advective transport as opposed to other drivers of imbalance. In particular, further studies of spatialized turbulent fluxes and improvements in the spatial representativeness of all energy budget components are needed, in addition to continued advection research, in order to fully address the challenge of energy balance non-closure.

# Appendix A

## Complete List of Cases

Case	Horizontal Gradient Method	Interpolation Distance [m]	Interpolation Direction	Interpolation Kernel	Stability Correction	Vertical Velocity
1	Interpolation	10	Upwind Downwind	thin_plate- _spline	Benoit (1977)	Sonic Anemometer
2	Interpolation	100	Upwind Downwind	thin_plate- _spline	Benoit (1977)	Sonic Anemometer
3	Interpolation	500	Upwind Downwind	thin_plate- _spline	Benoit (1977)	Sonic Anemometer
4	Interpolation	1000	Upwind Downwind	thin_plate- _spline	Benoit (1977)	Sonic Anemometer
5	Interpolation	5000	Upwind Downwind	thin_plate- _spline	Benoit (1977)	Sonic Anemometer
6	Interpolation	10	NSEW	thin_plate- _spline	Benoit (1977)	Sonic Anemometer
7	Interpolation	100	NSEW	thin_plate- _spline	Benoit (1977)	Sonic Anemometer
8	Interpolation	500	NSEW	thin_plate- _spline	Benoit (1977)	Sonic Anemometer
9	Interpolation	1000	NSEW	thin_plate- _spline	Benoit (1977)	Sonic Anemometer
10	Interpolation	5000	NSEW	thin_plate- _spline	Benoit (1977)	Sonic Anemometer
11	Interpolation	10	Upwind Downwind	linear	Benoit (1977)	Sonic Anemometer
12	Interpolation	100	Upwind Downwind	linear	Benoit (1977)	Sonic Anemometer

*Continued on the next page...*

Case	Horizontal Gradient Method	Interpolation Distance [m]	Interpolation Direction	Interpolation Kernel	Stability Correction	Vertical Velocity
13	Interpolation	500	Upwind Downwind	linear	Benoit (1977)	Sonic Anemometer
14	Interpolation	1000	Upwind Downwind	linear	Benoit (1977)	Sonic Anemometer
15	Interpolation	5000	Upwind Downwind	linear	Benoit (1977)	Sonic Anemometer
16	Interpolation	10	NSEW	linear	Benoit (1977)	Sonic Anemometer
17	Interpolation	100	NSEW	linear	Benoit (1977)	Sonic Anemometer
18	Interpolation	500	NSEW	linear	Benoit (1977)	Sonic Anemometer
19	Interpolation	1000	NSEW	linear	Benoit (1977)	Sonic Anemometer
20	Interpolation	5000	NSEW	linear	Benoit (1977)	Sonic Anemometer
21	Interpolation	10	Upwind Downwind	cubic	Benoit (1977)	Sonic Anemometer
22	Interpolation	100	Upwind Downwind	cubic	Benoit (1977)	Sonic Anemometer
23	Interpolation	500	Upwind Downwind	cubic	Benoit (1977)	Sonic Anemometer
24	Interpolation	1000	Upwind Downwind	cubic	Benoit (1977)	Sonic Anemometer
25	Interpolation	5000	Upwind Downwind	cubic	Benoit (1977)	Sonic Anemometer
26	Interpolation	10	NSEW	cubic	Benoit (1977)	Sonic Anemometer
27	Interpolation	100	NSEW	cubic	Benoit (1977)	Sonic Anemometer
28	Interpolation	500	NSEW	cubic	Benoit (1977)	Sonic Anemometer
29	Interpolation	1000	NSEW	cubic	Benoit (1977)	Sonic Anemometer
30	Interpolation	5000	NSEW	cubic	Benoit (1977)	Sonic Anemometer
31	Interpolation	10	Upwind Downwind	quintic	Benoit (1977)	Sonic Anemometer
32	Interpolation	100	Upwind Downwind	quintic	Benoit (1977)	Sonic Anemometer
33	Interpolation	500	Upwind Downwind	quintic	Benoit (1977)	Sonic Anemometer
34	Interpolation	1000	Upwind Downwind	quintic	Benoit (1977)	Sonic Anemometer
35	Interpolation	5000	Upwind Downwind	quintic	Benoit (1977)	Sonic Anemometer

*Continued on the next page...*

Case	Horizontal Gradient Method	Interpolation Distance [m]	Interpolation Direction	Interpolation Kernel	Stability Correction	Vertical Velocity
36	Interpolation	10	NSEW	quintic	Benoit (1977)	Sonic Anemometer
37	Interpolation	100	NSEW	quintic	Benoit (1977)	Sonic Anemometer
38	Interpolation	500	NSEW	quintic	Benoit (1977)	Sonic Anemometer
39	Interpolation	1000	NSEW	quintic	Benoit (1977)	Sonic Anemometer
40	Interpolation	5000	NSEW	quintic	Benoit (1977)	Sonic Anemometer
41	Interpolation	10	Upwind Downwind	multiquadric	Benoit (1977)	Sonic Anemometer
42	Interpolation	100	Upwind Downwind	multiquadric	Benoit (1977)	Sonic Anemometer
43	Interpolation	500	Upwind Downwind	multiquadric	Benoit (1977)	Sonic Anemometer
44	Interpolation	1000	Upwind Downwind	multiquadric	Benoit (1977)	Sonic Anemometer
45	Interpolation	5000	Upwind Downwind	multiquadric	Benoit (1977)	Sonic Anemometer
46	Interpolation	10	NSEW	multiquadric	Benoit (1977)	Sonic Anemometer
47	Interpolation	100	NSEW	multiquadric	Benoit (1977)	Sonic Anemometer
48	Interpolation	500	NSEW	multiquadric	Benoit (1977)	Sonic Anemometer
49	Interpolation	1000	NSEW	multiquadric	Benoit (1977)	Sonic Anemometer
50	Interpolation	5000	NSEW	multiquadric	Benoit (1977)	Sonic Anemometer
51	Interpolation	10	Upwind Downwind	thin_plate-spline	NA	Sonic Anemometer
52	Interpolation	100	Upwind Downwind	thin_plate-spline	NA	Sonic Anemometer
53	Interpolation	500	Upwind Downwind	thin_plate-spline	NA	Sonic Anemometer
54	Interpolation	1000	Upwind Downwind	thin_plate-spline	NA	Sonic Anemometer
55	Interpolation	5000	Upwind Downwind	thin_plate-spline	NA	Sonic Anemometer
56	Interpolation	10	NSEW	thin_plate-spline	NA	Sonic Anemometer
57	Interpolation	100	NSEW	thin_plate-spline	NA	Sonic Anemometer
58	Interpolation	500	NSEW	thin_plate-spline	NA	Sonic Anemometer

*Continued on the next page...*

Case	Horizontal Gradient Method	Interpolation Distance [m]	Interpolation Direction	Interpolation Kernel	Stability Correction	Vertical Velocity
59	Interpolation	1000	NSEW	thin_plate_spline	NA	Sonic Anemometer
60	Interpolation	5000	NSEW	thin_plate_spline	NA	Sonic Anemometer
61	Interpolation	10	Upwind Downwind	linear	NA	Sonic Anemometer
62	Interpolation	100	Upwind Downwind	linear	NA	Sonic Anemometer
63	Interpolation	500	Upwind Downwind	linear	NA	Sonic Anemometer
64	Interpolation	1000	Upwind Downwind	linear	NA	Sonic Anemometer
65	Interpolation	5000	Upwind Downwind	linear	NA	Sonic Anemometer
66	Interpolation	10	NSEW	linear	NA	Sonic Anemometer
67	Interpolation	100	NSEW	linear	NA	Sonic Anemometer
68	Interpolation	500	NSEW	linear	NA	Sonic Anemometer
69	Interpolation	1000	NSEW	linear	NA	Sonic Anemometer
70	Interpolation	5000	NSEW	linear	NA	Sonic Anemometer
71	Interpolation	10	Upwind Downwind	cubic	NA	Sonic Anemometer
72	Interpolation	100	Upwind Downwind	cubic	NA	Sonic Anemometer
73	Interpolation	500	Upwind Downwind	cubic	NA	Sonic Anemometer
74	Interpolation	1000	Upwind Downwind	cubic	NA	Sonic Anemometer
75	Interpolation	5000	Upwind Downwind	cubic	NA	Sonic Anemometer
76	Interpolation	10	NSEW	cubic	NA	Sonic Anemometer
77	Interpolation	100	NSEW	cubic	NA	Sonic Anemometer
78	Interpolation	500	NSEW	cubic	NA	Sonic Anemometer
79	Interpolation	1000	NSEW	cubic	NA	Sonic Anemometer
80	Interpolation	5000	NSEW	cubic	NA	Sonic Anemometer
81	Interpolation	10	Upwind Downwind	quintic	NA	Sonic Anemometer

*Continued on the next page...*

Case	Horizontal Gradient Method	Interpolation Distance [m]	Interpolation Direction	Interpolation Kernel	Stability Correction	Vertical Velocity
82	Interpolation	100	Upwind Downwind	quintic	NA	Sonic Anemometer
83	Interpolation	500	Upwind Downwind	quintic	NA	Sonic Anemometer
84	Interpolation	1000	Upwind Downwind	quintic	NA	Sonic Anemometer
85	Interpolation	5000	Upwind Downwind	quintic	NA	Sonic Anemometer
86	Interpolation	10	NSEW	quintic	NA	Sonic Anemometer
87	Interpolation	100	NSEW	quintic	NA	Sonic Anemometer
88	Interpolation	500	NSEW	quintic	NA	Sonic Anemometer
89	Interpolation	1000	NSEW	quintic	NA	Sonic Anemometer
90	Interpolation	5000	NSEW	quintic	NA	Sonic Anemometer
91	Interpolation	10	Upwind Downwind	multiquadric	NA	Sonic Anemometer
92	Interpolation	100	Upwind Downwind	multiquadric	NA	Sonic Anemometer
93	Interpolation	500	Upwind Downwind	multiquadric	NA	Sonic Anemometer
94	Interpolation	1000	Upwind Downwind	multiquadric	NA	Sonic Anemometer
95	Interpolation	5000	Upwind Downwind	multiquadric	NA	Sonic Anemometer
96	Interpolation	10	NSEW	multiquadric	NA	Sonic Anemometer
97	Interpolation	100	NSEW	multiquadric	NA	Sonic Anemometer
98	Interpolation	500	NSEW	multiquadric	NA	Sonic Anemometer
99	Interpolation	1000	NSEW	multiquadric	NA	Sonic Anemometer
100	Interpolation	5000	NSEW	multiquadric	NA	Sonic Anemometer
101	gradavg	NA	NA	NA	NA	Sonic Anemometer
102	gradavg	NA	NA	NA	NA	Sonic Anemometer
103	Interpolation	10	Upwind Downwind	thin_plate-spline	Benoit (1977)	Continuity
104	Interpolation	100	Upwind Downwind	thin_plate-spline	Benoit (1977)	Continuity

*Continued on the next page...*

Case	Horizontal Gradient Method	Interpolation Distance [m]	Interpolation Direction	Interpolation Kernel	Stability Correction	Vertical Velocity
105	Interpolation	500	Upwind Downwind	thin_plate_spline	Benoit (1977)	Continuity
106	Interpolation	1000	Upwind Downwind	thin_plate_spline	Benoit (1977)	Continuity
107	Interpolation	5000	Upwind Downwind	thin_plate_spline	Benoit (1977)	Continuity
108	Interpolation	10	NSEW	thin_plate_spline	Benoit (1977)	Continuity
109	Interpolation	100	NSEW	thin_plate_spline	Benoit (1977)	Continuity
110	Interpolation	500	NSEW	thin_plate_spline	Benoit (1977)	Continuity
111	Interpolation	1000	NSEW	thin_plate_spline	Benoit (1977)	Continuity
112	Interpolation	5000	NSEW	thin_plate_spline	Benoit (1977)	Continuity
113	Interpolation	10	Upwind Downwind	linear	Benoit (1977)	Continuity
114	Interpolation	100	Upwind Downwind	linear	Benoit (1977)	Continuity
115	Interpolation	500	Upwind Downwind	linear	Benoit (1977)	Continuity
116	Interpolation	1000	Upwind Downwind	linear	Benoit (1977)	Continuity
117	Interpolation	5000	Upwind Downwind	linear	Benoit (1977)	Continuity
118	Interpolation	10	NSEW	linear	Benoit (1977)	Continuity
119	Interpolation	100	NSEW	linear	Benoit (1977)	Continuity
120	Interpolation	500	NSEW	linear	Benoit (1977)	Continuity
121	Interpolation	1000	NSEW	linear	Benoit (1977)	Continuity
122	Interpolation	5000	NSEW	linear	Benoit (1977)	Continuity
123	Interpolation	10	Upwind Downwind	cubic	Benoit (1977)	Continuity
124	Interpolation	100	Upwind Downwind	cubic	Benoit (1977)	Continuity
125	Interpolation	500	Upwind Downwind	cubic	Benoit (1977)	Continuity
126	Interpolation	1000	Upwind Downwind	cubic	Benoit (1977)	Continuity
127	Interpolation	5000	Upwind Downwind	cubic	Benoit (1977)	Continuity

*Continued on the next page...*

Case	Horizontal Gradient Method	Interpolation Distance [m]	Interpolation Direction	Interpolation Kernel	Stability Correction	Vertical Velocity
128	Interpolation	10	NSEW	cubic	Benoit (1977)	Continuity
129	Interpolation	100	NSEW	cubic	Benoit (1977)	Continuity
130	Interpolation	500	NSEW	cubic	Benoit (1977)	Continuity
131	Interpolation	1000	NSEW	cubic	Benoit (1977)	Continuity
132	Interpolation	5000	NSEW	cubic	Benoit (1977)	Continuity
133	Interpolation	10	Upwind Downwind	quintic	Benoit (1977)	Continuity
134	Interpolation	100	Upwind Downwind	quintic	Benoit (1977)	Continuity
135	Interpolation	500	Upwind Downwind	quintic	Benoit (1977)	Continuity
136	Interpolation	1000	Upwind Downwind	quintic	Benoit (1977)	Continuity
137	Interpolation	5000	Upwind Downwind	quintic	Benoit (1977)	Continuity
138	Interpolation	10	NSEW	quintic	Benoit (1977)	Continuity
139	Interpolation	100	NSEW	quintic	Benoit (1977)	Continuity
140	Interpolation	500	NSEW	quintic	Benoit (1977)	Continuity
141	Interpolation	1000	NSEW	quintic	Benoit (1977)	Continuity
142	Interpolation	5000	NSEW	quintic	Benoit (1977)	Continuity
143	Interpolation	10	Upwind Downwind	multiquadric	Benoit (1977)	Continuity
144	Interpolation	100	Upwind Downwind	multiquadric	Benoit (1977)	Continuity
145	Interpolation	500	Upwind Downwind	multiquadric	Benoit (1977)	Continuity
146	Interpolation	1000	Upwind Downwind	multiquadric	Benoit (1977)	Continuity
147	Interpolation	5000	Upwind Downwind	multiquadric	Benoit (1977)	Continuity
148	Interpolation	10	NSEW	multiquadric	Benoit (1977)	Continuity
149	Interpolation	100	NSEW	multiquadric	Benoit (1977)	Continuity
150	Interpolation	500	NSEW	multiquadric	Benoit (1977)	Continuity

*Continued on the next page...*

Case	Horizontal Gradient Method	Interpolation Distance [m]	Interpolation Direction	Interpolation Kernel	Stability Correction	Vertical Velocity
151	Interpolation	1000	NSEW	multiquadric	Benoit (1977)	Continuity
152	Interpolation	5000	NSEW	multiquadric	Benoit (1977)	Continuity
153	Interpolation	10	Upwind Downwind	thin_plate_spline	NA	Continuity
154	Interpolation	100	Upwind Downwind	thin_plate_spline	NA	Continuity
155	Interpolation	500	Upwind Downwind	thin_plate_spline	NA	Continuity
156	Interpolation	1000	Upwind Downwind	thin_plate_spline	NA	Continuity
157	Interpolation	5000	Upwind Downwind	thin_plate_spline	NA	Continuity
158	Interpolation	10	NSEW	thin_plate_spline	NA	Continuity
159	Interpolation	100	NSEW	thin_plate_spline	NA	Continuity
160	Interpolation	500	NSEW	thin_plate_spline	NA	Continuity
161	Interpolation	1000	NSEW	thin_plate_spline	NA	Continuity
162	Interpolation	5000	NSEW	thin_plate_spline	NA	Continuity
163	Interpolation	10	Upwind Downwind	linear	NA	Continuity
164	Interpolation	100	Upwind Downwind	linear	NA	Continuity
165	Interpolation	500	Upwind Downwind	linear	NA	Continuity
166	Interpolation	1000	Upwind Downwind	linear	NA	Continuity
167	Interpolation	5000	Upwind Downwind	linear	NA	Continuity
168	Interpolation	10	NSEW	linear	NA	Continuity
169	Interpolation	100	NSEW	linear	NA	Continuity
170	Interpolation	500	NSEW	linear	NA	Continuity
171	Interpolation	1000	NSEW	linear	NA	Continuity
172	Interpolation	5000	NSEW	linear	NA	Continuity
173	Interpolation	10	Upwind Downwind	cubic	NA	Continuity

*Continued on the next page...*

Case	Horizontal Gradient Method	Interpolation Distance [m]	Interpolation Direction	Interpolation Kernel	Stability Correction	Vertical Velocity
174	Interpolation	100	Upwind Downwind	cubic	NA	Continuity
175	Interpolation	500	Upwind Downwind	cubic	NA	Continuity
176	Interpolation	1000	Upwind Downwind	cubic	NA	Continuity
177	Interpolation	5000	Upwind Downwind	cubic	NA	Continuity
178	Interpolation	10	NSEW	cubic	NA	Continuity
179	Interpolation	100	NSEW	cubic	NA	Continuity
180	Interpolation	500	NSEW	cubic	NA	Continuity
181	Interpolation	1000	NSEW	cubic	NA	Continuity
182	Interpolation	5000	NSEW	cubic	NA	Continuity
183	Interpolation	10	Upwind Downwind	quintic	NA	Continuity
184	Interpolation	100	Upwind Downwind	quintic	NA	Continuity
185	Interpolation	500	Upwind Downwind	quintic	NA	Continuity
186	Interpolation	1000	Upwind Downwind	quintic	NA	Continuity
187	Interpolation	5000	Upwind Downwind	quintic	NA	Continuity
188	Interpolation	10	NSEW	quintic	NA	Continuity
189	Interpolation	100	NSEW	quintic	NA	Continuity
190	Interpolation	500	NSEW	quintic	NA	Continuity
191	Interpolation	1000	NSEW	quintic	NA	Continuity
192	Interpolation	5000	NSEW	quintic	NA	Continuity
193	Interpolation	10	Upwind Downwind	multiquadric	NA	Continuity
194	Interpolation	100	Upwind Downwind	multiquadric	NA	Continuity
195	Interpolation	500	Upwind Downwind	multiquadric	NA	Continuity
196	Interpolation	1000	Upwind Downwind	multiquadric	NA	Continuity

*Continued on the next page...*

Case	Horizontal Gradient Method	Interpolation Distance [m]	Interpolation Direction	Interpolation Kernel	Stability Correction	Vertical Velocity
197	Interpolation	5000	Upwind Downwind	multiquadric	NA	Continuity
198	Interpolation	10	NSEW	multiquadric	NA	Continuity
199	Interpolation	100	NSEW	multiquadric	NA	Continuity
200	Interpolation	500	NSEW	multiquadric	NA	Continuity
201	Interpolation	1000	NSEW	multiquadric	NA	Continuity
202	Interpolation	5000	NSEW	multiquadric	NA	Continuity
203	gradavg	NA	NA	NA	NA	Continuity
204	gradavg	NA	NA	NA	NA	Continuity

---

TABLE A.1: List of all advective flux variations tested.

---

# Bibliography

- Aubinet, M., P. Berbigier, C. Bernhofer, A. Cescatti, C. Feigenwinter, A. Granier, T. Grünwald, K. Havrankova, B. Heinesch, B. Longdoz, B. Marcolla, L. Montagnani, and P. Sedlak, 2005: Comparing CO<sub>2</sub> Storage and Advection Conditions at Night at Different Carboeuroflux Sites. *Boundary-Layer Meteorology*, **116**, 63–93, doi:10.1007/s10546-004-7091-8.  
URL <http://link.springer.com/10.1007/s10546-004-7091-8>
- Aubinet, M., B. Heinesch, and M. Yernaux, 2003: Horizontal and vertical co<sub>2</sub> advection in a sloping forest. *Boundary-Layer Meteorology*, **108**, 397–417, doi:10.1023/A:1024168428135.  
URL <https://doi.org/10.1023/A:1024168428135>
- Baldocchi, D. D., 2003: Assessing the eddy covariance technique for evaluating carbon dioxide exchange rates of ecosystems: past, present and future. *Global Change Biology*, **9**, 479–492, doi:10.1046/j.1365-2486.2003.00629.x.  
URL <https://onlinelibrary.wiley.com/doi/10.1046/j.1365-2486.2003.00629.x>
- Barr, A., K. Morgenstern, T. Black, J. McCaughey, and Z. Nestic, 2006: Surface energy balance closure by the eddy-covariance method above three boreal forest stands and implications for the measurement of the CO<sub>2</sub> flux. *Agricultural and Forest Meteorology*, **140**, 322–337, doi:10.1016/j.agrformet.2006.08.007.  
URL <https://linkinghub.elsevier.com/retrieve/pii/S0168192306002292>
- Benoit, R., 1977: On the integral of the surface layer profile-gradient functions. *Journal of Applied Meteorology and Climatology*, **16**, 859 – 860, doi:10.1175/1520-0450(1977)016<0859:OTIOTS>2.0.CO;2.  
URL [https://journals.ametsoc.org/view/journals/apme/16/8/1520-0450\\_1977\\_016\\_0859\\_otiots\\_2\\_0\\_co\\_2.xml](https://journals.ametsoc.org/view/journals/apme/16/8/1520-0450_1977_016_0859_otiots_2_0_co_2.xml)
- Butterworth, B. J., A. R. Desai, D. Durden, H. Kadum, D. LaLuzerne, M. Mauder, S. Metzger, S. Paleri, and L. Wanner, 2024: Characterizing energy balance closure over a heterogeneous ecosystem using multi-tower eddy covariance. *Frontiers in Earth Science*, **11**, doi:10.3389/feart.2023.1251138.  
URL <https://www.frontiersin.org/journals/earth-science/articles/10.3389/feart.2023.1251138>
- Butterworth, B. J., A. R. Desai, P. A. Townsend, G. W. Petty, C. G. Andresen, T. H. Bertram, E. L. Kruger, J. K. Mineau, E. R. Olson, S. Paleri, R. A. Pertzborn, C. Pettersen, P. C. Stoy, J. E. Thom, M. P. Vermeuel, T. J. Wagner, D. B. Wright, T. Zheng, S. Metzger, M. D. Schwartz, T. J. Iglinski, M. Mauder, J. Speidel, H. Vogelmann, L. Wanner, T. J. Augustine, W. O. J. Brown, S. P. Oncley, M. Buban, T. R. Lee, P. Cleary, D. J. Durden, C. R. Florian, K. Lantz, L. D. Riihimaki, J. Sedlar, T. P. Meyers, D. M. Plummer, E. R. Guzman, E. N. Smith, M. Sühling, D. D. Turner, Z. Wang, L. D. White, and J. M. Wilczak, 2021: Connecting land–atmosphere interactions to surface heterogeneity in cheesehead19. *Bulletin of the American Meteorological Society*, **102**, E421 – E445, doi:10.1175/BAMS-D-19-0346.1.  
URL <https://journals.ametsoc.org/view/journals/bams/102/2/BAMS-D-19-0346.1.xml>

- Campbell, G. S. and J. M. Norman, 1998: *Wind*, Springer New York, New York, NY. 63–75.  
URL [https://doi.org/10.1007/978-1-4612-1626-1\\_5](https://doi.org/10.1007/978-1-4612-1626-1_5)
- Cuxart, J., B. Wrenger, D. Martínez-Villagrasa, J. Reuder, M. O. Jonassen, M. A. Jiménez, M. Lothon, F. Lohou, O. Hartogensis, J. Dünnermann, L. Conangla, and A. Garai, 2016: Estimation of the advection effects induced by surface heterogeneities in the surface energy budget. *Atmospheric Chemistry and Physics*, **16**, 9489–9504, doi:10.5194/acp-16-9489-2016.  
URL <https://acp.copernicus.org/articles/16/9489/2016/>
- Desjardins, R. L., J. I. MacPherson, L. Mahrt, P. Schuepp, E. Pattey, H. Neumann, D. Baldocchi, S. Wofsy, D. Fitzjarrald, H. McCaughey, and D. W. Joiner, 1997: Scaling up flux measurements for the boreal forest using aircraft-tower combinations. *Journal of Geophysical Research: Atmospheres*, **102**, 29125–29133, doi:10.1029/97JD00278.  
URL <https://agupubs.onlinelibrary.wiley.com/doi/10.1029/97JD00278>
- Eder, F., F. De Roo, K. Kohnert, R. L. Desjardins, H. P. Schmid, and M. Mauder, 2014: Evaluation of two energy balance closure parametrizations. *Boundary-Layer Meteorology*, **151**, 195–219, doi:10.1007/s10546-013-9904-0.  
URL <https://doi.org/10.1007/s10546-013-9904-0>
- Eder, F. and M. Mauder, 2015: Secondary circulations at a solitary forest surrounded by semi-arid shrubland and their impact on eddy-covariance measurements. *Agricultural and Forest Meteorology*.
- Feigenwinter, C., C. Bernhofer, U. Eichelmann, B. Heinesch, M. Hertel, D. Janous, O. Kolle, F. Lagergren, A. Lindroth, S. Minerbi, U. Moderow, M. Mölder, L. Montagnani, R. Queck, C. Rebmann, P. Vestin, M. Yernaux, M. Zeri, W. Ziegler, and M. Aubinet, 2008: Comparison of horizontal and vertical advective CO<sub>2</sub> fluxes at three forest sites. *Agricultural and Forest Meteorology*, **148**, 12–24, doi:10.1016/j.agrformet.2007.08.013.  
URL <https://linkinghub.elsevier.com/retrieve/pii/S016819230700233X>
- Finnigan, J. J. and Y. Brunet, 1995: *Turbulent airflow in forests on flat and hilly terrain*, Cambridge University Press. 3–40.
- Finnigan, J. J., R. Clement, Y. Malhi, R. Leuning, and H. Cleugh, 2003: A Re-Evaluation of Long-Term Flux Measurement Techniques Part I: Averaging and Coordinate Rotation. *Boundary-Layer Meteorology*, **107**, 1–48, doi:10.1023/A:1021554900225.  
URL <http://link.springer.com/10.1023/A:1021554900225>
- Fisher, R. A. and C. D. Koven, 2020: Perspectives on the Future of Land Surface Models and the Challenges of Representing Complex Terrestrial Systems. *Journal of Advances in Modeling Earth Systems*, **12**, e2018MS001453, doi:10.1029/2018MS001453.  
URL <https://agupubs.onlinelibrary.wiley.com/doi/10.1029/2018MS001453>
- Foken, T., 2008: THE ENERGY BALANCE CLOSURE PROBLEM: AN OVERVIEW. *Ecological Applications*, **18**, 1351–1367, doi:10.1890/06-0922.1.  
URL <https://esajournals.onlinelibrary.wiley.com/doi/10.1890/06-0922.1>
- Foken, T. and B. Wichura, 1996: Tools for quality assessment of surface-based flux measurements. *Agricultural and Forest Meteorology*, **78**, 83–105, doi:10.1016/0168-1923(95)02248-1.  
URL <https://linkinghub.elsevier.com/retrieve/pii/0168192395022481>
- Foken, T., F. Wimmer, M. Mauder, C. Thomas, and C. Liebenthal, 2006: Some aspects of the energy balance closure problem. *Atmospheric Chemistry and Physics*, **6**, 4395–4402, doi:10.5194/acp-6-4395-2006.  
URL <https://acp.copernicus.org/articles/6/4395/2006/>

- Franssen, H. H., R. Stöckli, I. Lehner, E. Rotenberg, and S. Seneviratne, 2010: Energy balance closure of eddy-covariance data: A multisite analysis for European FLUXNET stations. *Agricultural and Forest Meteorology*, **150**, 1553–1567, doi:10.1016/j.agrformet.2010.08.005.  
URL <https://linkinghub.elsevier.com/retrieve/pii/S0168192310002194>
- Garcia-Santos, V., J. Cuxart, M. A. Jimenez, D. Martinez-Villagrasa, G. Simo, R. Picos, and V. Caselles, 2019: Study of Temperature Heterogeneities at Sub-Kilometric Scales and Influence on Surface–Atmosphere Energy Interactions. *IEEE Transactions on Geoscience and Remote Sensing*, **57**, 640–654, doi:10.1109/TGRS.2018.2859182.  
URL <https://ieeexplore.ieee.org/document/8430647/>
- Haverd, V., M. Cuntz, R. Leuning, and H. Keith, 2007: Air and biomass heat storage fluxes in a forest canopy: Calculation within a soil vegetation atmosphere transfer model. *Agricultural and Forest Meteorology*, **147**, 125–139, doi:10.1016/j.agrformet.2007.07.006.  
URL <https://linkinghub.elsevier.com/retrieve/pii/S0168192307001876>
- Higgins, C. W., E. Pardyjak, M. Froidevaux, V. Simeonov, and M. B. Parlange, 2013: Measured and Estimated Water Vapor Advection in the Atmospheric Surface Layer. *Journal of Hydrometeorology*, **14**, 1966–1972, doi:10.1175/JHM-D-12-0166.1.  
URL <http://journals.ametsoc.org/doi/10.1175/JHM-D-12-0166.1>
- Inagaki, A., M. O. Letzel, S. Raasch, and M. Kanda, 2006: Impact of Surface Heterogeneity on Energy Imbalance: A Study Using LES. *Journal of the Meteorological Society of Japan. Ser. II*, **84**, 187–198, doi:10.2151/jmsj.84.187.  
URL [http://www.jstage.jst.go.jp/article/jmsj/84/1/84\\_1\\_187/\\_article](http://www.jstage.jst.go.jp/article/jmsj/84/1/84_1_187/_article)
- Inoue, E., 1963: On the turbulent structure of airflow within crop canopies. *Journal of the Meteorological Society of Japan. Ser. II*, **41**, 317–326, doi:10.2151/jmsj1923.41.6317.
- Kanda, M., A. Inagaki, M. O. Letzel, S. Raasch, and T. Watanabe, 2004: LES Study of the Energy Imbalance Problem with Eddy Covariance Fluxes. *Boundary-Layer Meteorology*, **110**, 381–404, doi:10.1023/B:BOUN.0000007225.45548.7a.  
URL <http://link.springer.com/10.1023/B:BOUN.0000007225.45548.7a>
- Katul, G. G., J. J. Finnigan, D. Poggi, R. Leuning, and S. E. Belcher, 2006: The Influence of Hilly Terrain on Canopy-Atmosphere Carbon Dioxide Exchange. *Boundary-Layer Meteorology*, **118**, 189–216, doi:10.1007/s10546-005-6436-2.  
URL <http://link.springer.com/10.1007/s10546-005-6436-2>
- Kochendorfer, J. and K. T. Paw U, 2011: Field estimates of scalar advection across a canopy edge. *Agricultural and Forest Meteorology*, **151**, 585–594, doi:10.1016/j.agrformet.2011.01.003.  
URL <https://linkinghub.elsevier.com/retrieve/pii/S0168192311000220>
- Lee, X., 1998: On micrometeorological observations of surface-air exchange over tall vegetation. *Agricultural and Forest Meteorology*, **91**, 39–49, doi:10.1016/S0168-1923(98)00071-9.  
URL <https://linkinghub.elsevier.com/retrieve/pii/S0168192398000719>
- Lee, X. and T. A. Black, 1993: Atmospheric turbulence within and above a douglas-fir stand. Part II: Eddy fluxes of sensible heat and water vapour. *Boundary-Layer Meteorology*, **64**, 369–389, doi:10.1007/BF00711706.  
URL <http://link.springer.com/10.1007/BF00711706>
- Lee, X. and X. Hu, 2002: Forest-Air Fluxes Of Carbon, Water And Energy Over Non-Flat Terrain. *Boundary-Layer Meteorology*, **103**, 277–301, doi:10.1023/A:1014508928693.  
URL <http://link.springer.com/10.1023/A:1014508928693>

- Leuning, R., E. Van Gorsel, W. J. Massman, and P. R. Isaac, 2012: Reflections on the surface energy imbalance problem. *Agricultural and Forest Meteorology*, **156**, 65–74, doi:10.1016/j.agrformet.2011.12.002. URL <https://linkinghub.elsevier.com/retrieve/pii/S016819231100339X>
- Lindroth, A., M. Mölder, and F. Lagergren, 2010: Heat storage in forest biomass improves energy balance closure. *Biogeosciences*, **7**, 301–313, doi:10.5194/bg-7-301-2010. URL <https://bg.copernicus.org/articles/7/301/2010/>
- Mahrt, L., J. Sun, D. Vickers, J. I. Macpherson, J. R. Pederson, and R. L. Desjardins, 1994: Observations of fluxes and inland breezes over a heterogeneous surface. *Journal of Atmospheric Sciences*, **51**, 2484 – 2499, doi:10.1175/1520-0469(1994)051;2484:OOFAIB;2.0.CO;2. URL [https://journals.ametsoc.org/view/journals/atsc/51/17/1520-0469\\_1994\\_051\\_2484\\_oofaib\\_2\\_0\\_co\\_2.xml](https://journals.ametsoc.org/view/journals/atsc/51/17/1520-0469_1994_051_2484_oofaib_2_0_co_2.xml)
- Massman, W. and X. Lee, 2002: Eddy covariance flux corrections and uncertainties in long-term studies of carbon and energy exchanges. *Agricultural and Forest Meteorology*, **113**, 121–144, doi:10.1016/S0168-1923(02)00105-3. URL <https://linkinghub.elsevier.com/retrieve/pii/S0168192302001053>
- Mauder, M., R. L. Desjardins, E. Pattey, and D. Worth, 2010: An Attempt to Close the Daytime Surface Energy Balance Using Spatially-Averaged Flux Measurements. *Boundary-Layer Meteorology*, **136**, 175–191, doi:10.1007/s10546-010-9497-9. URL <http://link.springer.com/10.1007/s10546-010-9497-9>
- Mauder, M. and T. Foken, 2006: Impact of post-field data processing on eddy covariance flux estimates and energy balance closure. *Meteorologische Zeitschrift*, **15**, 597–609, doi:10.1127/0941-2948/2006/0167. URL [http://www.schweizerbart.de/papers/metz/detail/15/55217/Impact\\_of\\_post\\_field\\_data\\_processing\\_on\\_eddy\\_covar?af=crossref](http://www.schweizerbart.de/papers/metz/detail/15/55217/Impact_of_post_field_data_processing_on_eddy_covar?af=crossref)
- Mauder, M., T. Foken, and J. Cuxart, 2020: Surface-Energy-Balance Closure over Land: A Review. *Boundary-Layer Meteorology*, **177**, 395–426, doi:10.1007/s10546-020-00529-6. URL <https://link.springer.com/10.1007/s10546-020-00529-6>
- Mauder, M., S. P. Oncley, R. Vogt, T. Weidinger, L. Ribeiro, C. Bernhofer, T. Foken, W. Kohsiek, H. A. R. De Bruin, and H. Liu, 2007: The energy balance experiment EBEX-2000. Part II: Intercomparison of eddy-covariance sensors and post-field data processing methods. *Boundary-Layer Meteorology*, **123**, 29–54, doi:10.1007/s10546-006-9139-4. URL <http://link.springer.com/10.1007/s10546-006-9139-4>
- McGloin, R., L. Šigut, K. Havránková, J. Dušek, M. Pavelka, and P. Sedlák, 2018: Energy balance closure at a variety of ecosystems in Central Europe with contrasting topographies. *Agricultural and Forest Meteorology*, **248**, 418–431, doi:10.1016/j.agrformet.2017.10.003. URL <https://linkinghub.elsevier.com/retrieve/pii/S0168192317303234>
- Metzger, M. and H. Holmes, 2007: Time Scales in the Unstable Atmospheric Surface Layer. *Boundary-Layer Meteorology*, **126**, 29–50, doi:10.1007/s10546-007-9219-0. URL <http://link.springer.com/10.1007/s10546-007-9219-0>
- Metzger, S., 2018: Surface-atmosphere exchange in a box: Making the control volume a suitable representation for in-situ observations. *Agricultural and Forest Meteorology*, **255**, 68–80, doi:10.1016/j.agrformet.2017.08.037. URL <https://linkinghub.elsevier.com/retrieve/pii/S0168192317302939>

- Meyers, T., 2004: An assessment of storage terms in the surface energy balance of maize and soybean. *Agricultural and Forest Meteorology*, **125**, 105–115, doi:10.1016/j.agrformet.2004.03.001.  
URL <https://linkinghub.elsevier.com/retrieve/pii/S0168192304000620>
- Moderow, U., C. Feigenwinter, and C. Bernhofer, 2007: Estimating the components of the sensible heat budget of a tall forest canopy in complex terrain. *Boundary-Layer Meteorology*, **123**, 99–120, doi:10.1007/s10546-006-9136-7.  
URL <http://link.springer.com/10.1007/s10546-006-9136-7>
- Moderow, U., T. Grünwald, R. Queck, U. Spank, and C. Bernhofer, 2021: Energy balance closure and advective fluxes at ADVEX sites. *Theoretical and Applied Climatology*, **143**, 761–779, doi:10.1007/s00704-020-03412-z.  
URL <http://link.springer.com/10.1007/s00704-020-03412-z>
- Moncrieff, J., J. Massheder, H. De Bruin, J. Elbers, T. Friborg, B. Heusinkveld, P. Kabat, S. Scott, H. Soegaard, and A. Verhoef, 1997: A system to measure surface fluxes of momentum, sensible heat, water vapour and carbon dioxide. *Journal of Hydrology*, **188–189**, 589–611, doi:10.1016/S0022-1694(96)03194-0.  
URL <https://linkinghub.elsevier.com/retrieve/pii/S0022169496031940>
- Moore, C. J., 1986: Frequency response corrections for eddy correlation systems. *Boundary-Layer Meteorology*, **37**, 17–35, doi:10.1007/BF00122754.  
URL <http://link.springer.com/10.1007/BF00122754>
- Morrison, T., M. Calaf, C. W. Higgins, S. A. Drake, A. Perelet, and E. Pardyjak, 2021: The impact of surface temperature heterogeneity on near-surface heat transport. *Boundary-Layer Meteorology*, **180**, 247–272, doi:10.1007/s10546-021-00624-2.  
URL <https://doi.org/10.1007/s10546-021-00624-2>
- Morrison, T. J., M. Calaf, and E. R. Pardyjak, 2023: A full three-dimensional surface energy balance over a desert playa. *Quarterly Journal of the Royal Meteorological Society*, **149**, 102–114, doi:https://doi.org/10.1002/qj.4397.  
URL <https://rmets.onlinelibrary.wiley.com/doi/abs/10.1002/qj.4397>
- Myneni, R., 2023: Viirs/npp leaf area index/fpar 8-day l4 global 500m sin grid v002. Accessed: 2024-11-22.  
URL <https://doi.org/10.5067/VIIRS/VNP15A2H.002>
- NCAR/EOL In-situ Sensing Facility and S. Oncley, 2021: Near/eol 5 minute isfs surface flux data, tilt corrected, geographic coordinate winds. Accessed: 2024-12-03.  
URL <https://doi.org/10.26023/43MF-NP8N-3Q0V>
- Novick, K., S. Brantley, C. F. Miniati, J. Walker, and J. Vose, 2014: Inferring the contribution of advection to total ecosystem scalar fluxes over a tall forest in complex terrain. *Agricultural and Forest Meteorology*, **185**, 1–13, doi:https://doi.org/10.1016/j.agrformet.2013.10.010.  
URL <https://www.sciencedirect.com/science/article/pii/S0168192313002785>
- Oncley, S. P., T. Foken, R. Vogt, W. Kohsiek, H. A. R. DeBruin, C. Bernhofer, A. Christen, E. V. Gorsel, D. Grantz, C. Feigenwinter, I. Lehner, C. Liebenthal, H. Liu, M. Mauder, A. Pitacco, L. Ribeiro, and T. Weidinger, 2007: The Energy Balance Experiment EBEX-2000. Part I: overview and energy balance. *Boundary-Layer Meteorology*, **123**, 1–28, doi:10.1007/s10546-007-9161-1.  
URL <http://link.springer.com/10.1007/s10546-007-9161-1>
- Paleri, S., L. Wanner, M. Sühring, A. Desai, M. Mauder, and S. Metzger, PREPRINT: Impact of surface heterogeneity induced secondary circulations on the atmospheric boundary layer. doi:10.21203/rs.3.rs-3439181/v1.

- Panin, G. N., G. Tetzlaff, and A. Raabe, 1998: Inhomogeneity of the Land Surface and Problems in the Parameterization of Surface Fluxes in Natural Conditions. *Theoretical and Applied Climatology*, **60**, 163–178, doi:10.1007/s007040050041.  
URL <http://link.springer.com/10.1007/s007040050041>
- Pielke, R. A., . Sr, R. Avissar, M. Raupach, A. J. Dolman, X. Zeng, and A. S. Denning, 1998: Interactions between the atmosphere and terrestrial ecosystems: influence on weather and climate. *Global Change Biology*, **4**, 461–475, doi:10.1046/j.1365-2486.1998.t01-1-00176.x.  
URL <https://onlinelibrary.wiley.com/doi/10.1046/j.1365-2486.1998.t01-1-00176.x>
- Schmid, H., 1997: Experimental design for flux measurements: matching scales of observations and fluxes. *Agricultural and Forest Meteorology*, **87**, 179–200, doi:10.1016/S0168-1923(97)00011-7.  
URL <https://linkinghub.elsevier.com/retrieve/pii/S0168192397000117>
- Steinfeld, G., M. O. Letzel, S. Raasch, M. Kanda, and A. Inagaki, 2007: Spatial representativeness of single tower measurements and the imbalance problem with eddy-covariance fluxes: results of a large-eddy simulation study. *Boundary-Layer Meteorology*, **123**, 77–98, doi:10.1007/s10546-006-9133-x.  
URL <http://link.springer.com/10.1007/s10546-006-9133-x>
- Stoy, P. C., M. Mauder, T. Foken, B. Marcolla, E. Boegh, A. Ibrom, M. A. Arain, A. Arneth, M. Aurela, C. Bernhofer, A. Cescatti, E. Dellwik, P. Duce, D. Gianelle, E. Van Gorsel, G. Kiely, A. Knohl, H. Margolis, H. McCaughey, L. Merbold, L. Montagnani, D. Papale, M. Reichstein, M. Saunders, P. Serrano-Ortiz, M. Sottocornola, D. Spano, F. Vaccari, and A. Varlagin, 2013: A data-driven analysis of energy balance closure across FLUXNET research sites: The role of landscape scale heterogeneity. *Agricultural and Forest Meteorology*, **171-172**, 137–152, doi:10.1016/j.agrformet.2012.11.004.  
URL <https://linkinghub.elsevier.com/retrieve/pii/S0168192312003413>
- Stull, R. B., 1988: *Similarity Theory*, Springer Netherlands, Dordrecht. 347–404.  
URL [https://doi.org/10.1007/978-94-009-3027-8\\_9](https://doi.org/10.1007/978-94-009-3027-8_9)
- Twine, T., W. Kustas, J. Norman, D. Cook, P. Houser, T. Meyers, J. Prueger, P. Starks, and M. Wesely, 2000: Correcting eddy-covariance flux underestimates over a grassland. *Agricultural and Forest Meteorology*, **103**, 279–300, doi:10.1016/S0168-1923(00)00123-4.  
URL <https://linkinghub.elsevier.com/retrieve/pii/S0168192300001234>
- Wang, T., J. Alfieri, K. Mallick, A. Arias-Ortiz, M. Anderson, J. B. Fisher, M. Girotto, D. Szutu, J. Verfaillie, and D. Baldocchi, 2024: How advection affects the surface energy balance and its closure at an irrigated alfalfa field. *Agricultural and Forest Meteorology*, **357**, 110196, doi:10.1016/j.agrformet.2024.110196.  
URL <https://linkinghub.elsevier.com/retrieve/pii/S0168192324003095>
- Wanner, L., M. Jung, S. Paleri, B. J. Butterworth, A. R. Desai, M. Sühling, and M. Mauder, 2024: Towards Energy-Balance Closure with a Model of Dispersive Heat Fluxes. *Boundary-Layer Meteorology*, **190**, 25, doi:10.1007/s10546-024-00868-8.  
URL <https://link.springer.com/10.1007/s10546-024-00868-8>
- Webb, E. K., G. I. Pearman, and R. Leuning, 1980: Correction of flux measurements for density effects due to heat and water vapour transfer. *Quarterly Journal of the Royal Meteorological Society*, **106**, 85–100, doi:10.1002/qj.49710644707.  
URL <https://rmets.onlinelibrary.wiley.com/doi/10.1002/qj.49710644707>
- Wilson, K., A. Goldstein, E. Falge, M. Aubinet, D. Baldocchi, P. Berbigier, C. Bernhofer, R. Ceulemans, H. Dolman, C. Field, A. Grelle, A. Ibrom, B. Law, A. Kowalski, T. Meyers, J. Moncrieff, R. Monson, W. Oechel, J. Tenhunen, R. Valentini, and S. Verma, 2002: Energy balance closure at FLUXNET sites. *Agricultural and Forest Meteorology*, **113**, 223–243, doi:10.1016/S0168-1923(02)00109-0.  
URL <https://linkinghub.elsevier.com/retrieve/pii/S0168192302001090>

- Xu, K., N. Pinguitha-Durden, H. Luo, D. Durden, C. Sturtevant, A. R. Desai, C. Florian, and S. Metzger, 2019: The eddy-covariance storage term in air: Consistent community resources improve flux measurement reliability. *Agricultural and Forest Meteorology*, **279**, 107734, doi:10.1016/j.agrformet.2019.107734. URL <https://linkinghub.elsevier.com/retrieve/pii/S0168192319303508>
- Xu, Z., Y. Ma, S. Liu, W. Shi, and J. Wang, 2017: Assessment of the Energy Balance Closure under Advective Conditions and Its Impact Using Remote Sensing Data. *Journal of Applied Meteorology and Climatology*, **56**, 127–140, doi:10.1175/JAMC-D-16-0096.1. URL <https://journals.ametsoc.org/view/journals/apme/56/1/jamc-d-16-0096.1.xml>
- Yi, C., 2008: Momentum Transfer within Canopies. *JOURNAL OF APPLIED METEOROLOGY AND CLIMATOLOGY*, **47**.
- Zhou, Y. and X. Li, 2019: Energy balance closures in diverse ecosystems of an endorheic river basin. *Agricultural and Forest Meteorology*, **274**, 118–131, doi:10.1016/j.agrformet.2019.04.019. URL <https://linkinghub.elsevier.com/retrieve/pii/S0168192319301650>